RESEARCH ARTICLE

Metal oxide stabilized zirconia modified bio-derived carbon nanosheets as efficient electrocatalysts for oxygen evolution reaction
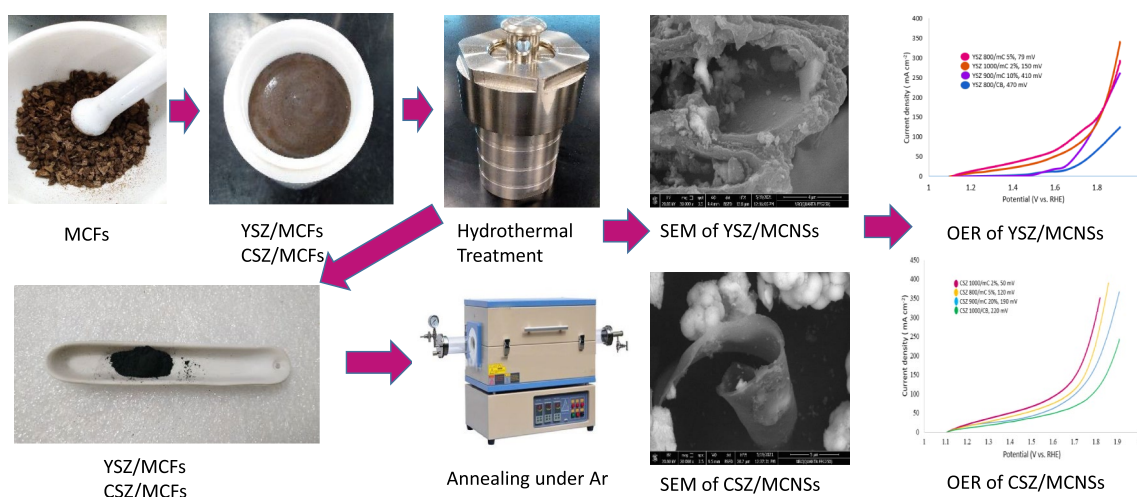
Menna M. Abo-Zeid[1] · Muhammad G. Abd El-Moghny[2] · H. Shawkey[3] · A. M. Daher[1] · Amr M. Abdelkader[4] · Mohamed S. El-Deab[2]

Abstract

Zirconia is a promising candidate for many applications, especially when stabilized with metal oxide nanoparticles such as yttria and ceria. Zirconium oxide-based materials supported on carbon nanomaterials have shown excellent performance electrocatalysts due to their outstanding catalytic activities and high stability. In this work, a one-pot hydrothermal method was used to prepare porous stabilized zirconia nanoparticles with yttria and ceria (YSZ and CSZ) anchored on carbon nanosheets derived from molasses fiber waste as a sustainable source and annealing at various temperatures (MCNSs). The prepared composites YSZ/MCNSs and CSZ/MCNSs exhibit superior oxygen evolution reaction performance in alkaline medium. Various physicochemical analysis techniques such as SEM, EDX, HR-TEM, BET, XRD and XPS are employed to characterize the designed catalysts. The results showed that the doping of molasses fibers exfoliated into 2D nanosheets controlled the growth of the YSZ particles into the nanosize and increased their crystallinity. This improves the electrochemical surface area and stability, and modulates the electronic structure of zirconium, yttrium and cerium which facilitate the adsorption of OH^- ions, and all contribute to the higher catalytic activity.

Graphical Abstract

MCFs → YSZ/MCFs CSZ/MCFs → Hydrothermal Treatment → SEM of YSZ/MCNSs → OER of YSZ/MCNSs

YSZ/MCFs CSZ/MCFs → Annealing under Ar → SEM of CSZ/MCNSs → OER of CSZ/MCNSs

Extended author information available on the last page of the article

Springer

1 Introduction

Recently, tremendous efforts have been made for the preparation of efficient catalysts for energy storage and conversion devices. The production of hydrogen gas is considered to be a green and sustainable source of energy. An important supplement of hydrogen energy is the electrochemical water splitting, with two half reactions involved, namely, hydrogen evolution reaction (HER) which occurs at the cathode and oxygen evolution reaction (OER) which occurs at the anode. Owing to the stepwise four-electron/proton transfer on the anodic side, the efficiency of the water splitting mainly depends on the rate of water oxidation, as the OER kinetics are more sluggish than the kinetics of HER [1, 2].

Furthermore, OER plays an important role in many electrochemical energy conversion systems, such as water splitting, fuel cells and metal-air batteries [3, 4]. Therefore, developing novel and efficient electrocatalysts is required to overcome the limited overall water electrolysis process. Until now, noble metal-based catalysts such as IrO_2 and RuO_2 are identified among the best catalysts for OER. However, their scarcity and high cost limit their large-scale application. Tremendous research has been made in recent years to develop non-precious cheap catalysts, with an increasing trend that focuses on using eco-friendly production methods [5, 6].

Transition metal oxides-based catalysts such as zirconia-based catalysts have been recently reported as attractive candidates to replace the noble metal-based catalysts for OER with better electrocatalytic activity. By tuning the composition, stabilizers, morphology, electronic and crystalline structures, their electrocatalytic performance can be enhanced.

Yttria stabilized zirconia (YSZ) has been most widely used in fuel cells, catalytic applications and various industrial applications. It's well-known that zirconia exhibits the monoclinic phase at room temperature, hence doping with low valence metals like Y^{3+} is supposed to stabilize the tetragonal phase in the nanocrystalline form. The tetragonal phase is considered to be rich in oxygen vacancies which is essential for the electrocatalysis [7].

Ceria or so-called Cerium oxide has attracted much attention worldwide due to its simple structure, abundance and excellent catalytic performance, and this in turn enables ceria to be used in various applications such as environmental catalysis, oxygen sensors and fuel cells [6, 8]. The high activity of Ceria-supported catalysts is due to the redox ability of ceria which could be enhanced by the formation of oxygen vacancy in ceria under catalytic conditions. Also, ceria can act as a good oxygen buffer due to its fluorite structure which makes it easier to switch between ⁺3 and ⁺ 4 oxidation states. It's well-known that Rh/CeO_2, Ru/CeO_2, Pd/CeO_2 catalysts are known to show outstanding catalytic activity towards oxygen evolution reaction (OER) in alkaline medium [8–10].

The synthesis of nanoparticles on conductive carbon materials has attracted much attention as efficient electrocatalysts. Nanosized zirconium oxide has been supported on graphitic carbon materials such as carbon black, carbon fibers, carbon nanotubes, and graphene sheets via various routes [11–13]. In addition, sustainable carbon sources from agricultural waste have been receiving increasing attention in the last few years. Fibers derived from natural sources present several advantages over synthetic fibers. They are abundant, biodegradable and renewable. Moreover, they have neutral emission of CO_2 which cause less environmental impact [14].

Furthermore, it was reported that, in the electrochemical testing process, the corrosion resistance and stability of transition metal materials used as electrocatalysts are improved by introducing cerium or ceria. Moreover, the interaction between zirconia and ceria can enhance the catalytic activity because of their dual function mechanism [15–17]. Doping of zirconia with yttria and ceria improves the stability of composite materials. These catalysts are considered to be of high efficiency, stability and also inexpensive, and that make them excellent candidates to be efficient electrocatalysts for OER. Also, it was found that ceria and carbon material support have a synergistic effect, which enhances the catalytic activity of the electrocatalyst. One of its benefits is its multivalent nature which helps in electron exchange between matrices and leads to excellent electronic structure tuning and so better OER performance. Tuning the composition, solid solution phase, and structure of the yttria and ceria stabilized zirconia (YSZ and CSZ) composites would enhance the concentration of oxygen vacancies and increase the specific surface area, thereby improving the catalytic activity of the OER electrocatalyst [7, 15–19].

In this paper, zirconia was doped and stabilized with ceria and yttria in two families of nanoparticles anchored on carbon nanosheets derived from natural molasses fibers (MCNSs) as efficient electrocatalysts for OER. The prepared composites showed enhanced electrocatalytic activities over traditional transition metal oxide-based catalysts.

2 Experimental section

2.1 Molasses fibers preparation

Extraction of the sugar cane fiber from the plant stem was performed according to the process reported in literature [14]. As the fiber's quality depends on the moisture content, a suitable drying under vacuum at 200 °C for 3 h was

required to obtain partial pyrolysis. Then it was followed by grinding of fibers in mortar and pestle.

2.2 Preparation of YSZ/MCNSs and CSZ/MCNSs composites via hydrothermal method

Two families of yttria and ceria stabilized zirconia anchored on molasses carbon nanosheets YSZ/MCNSs and CSZ/MCNSs composites have been prepared. YSZ and CSZ nanoparticles were prepared by previously published one-pot hydrothermal method [11, 16].

The aim of this work is to optimize the amount of molasses carbon and annealing temperature of the YSZ and CSZ composites. In order to achieve that, two families of composites were prepared, YSZ/MCNSs and CSZ/MCNSs with different molasses carbon weight% and annealed at three different temperatures. The synthesized samples were denoted as YSZ X/mC Y and CSZ X/mC Y, where X is the calcination temperature; 800, 900 and 1000 °C and Y is the molasses carbon weight ratios; 2, 5, 10, 20 wt%).

To synthesize YSZ/MCNSs and CSZ/MCNS composites with variable molasses carbon weight ratios, dried and ground molasses fibers were added to the obtained solution of the yttria, ceria and zirconia salts according to the weight percent of each composite while stirring. The obtained gels was then employed for hydrothermal treatment followed by drying in vacuum and finally thermal annealing process in Argon environment in a tube furnace at different temperatures 800, 900 and 1000 °C for 2 h with heating rate of 2 degree per minute to maintain equilibrium heating and cooling and to prevent oxidation of carbon into carbon dioxide. The annealing process was followed by leaching with concentrated HCl at 80 °C. This introduced more porosity to the structures and decreased the particle size. The product was then washed thoroughly with deionized water, filtered and subsequently dried at 100 °C for 12 h in vacuum.

2.3 Fabrication of blank YSZ/CB and CSZ/CB composites

Blank YSZ and CSZ composites were prepared via the same method. The difference was that the molasses carbon was replaced by carbon black in the electrode preparation step.

3 The working electrodes preparation

3.1 Catalyst preparation of the YSZ/MCNSs and CSZ/MCNSs composites

The as-prepared YSZ/MCNSs and CSZ/MCNSs composites were in powder form, so it was essential to cast the powder into a film to test its OER activity. The working electrodes were prepared according to that procedure reported in literature and the used conductive substrate was copper foil [13–16].

To acquire the 8 mol% YSZ annealed at 800 °C with 2 wt% molasses CNSs working electrode; 50 mg YSZ annealed at 800 °C/2 wt% molasses CNSs powder, 5.56 mg PVDF and 10 µL NMP were mixed and ground in mortar and pestle. Then, the obtained homogeneous ink was coated onto a bare Cu foil substrate with a geometric area of 1.13 cm^2, which was appointed as YSZ 800/mC 2% for comparison with the other samples. Then, the best electrocatalytic activity sample of each group was chosen to be compared with that of the other ones as shown in Fig. S1 for the YSZ/MCNSs group of catalysts and Fig. S2 for the CSZ/MCNSs group of catalysts.

3.2 Catalyst preparation of the blank samples without MCNSs

Blank samples were prepared via the same preparation procedure while using carbon black (Vulcan XC-72R) as the conductive agent using the preparation ratios; 90 wt% of active material, 5 wt% of binder and 5 wt% of carbon black. To acquire the YSZ/carbon black (YSZ/CB) electrode, 100 mg YSZ composites powder annealed at 800, 900 or 1000 °C, 5.55 mg carbon black (Vulcan XC-72R), 5.56 mg PVDF and 10 µL NMP were mixed and ground in mortar and pestle. Next, the obtained homogeneous ink was coated onto a bare Cu foil substrate with a geometric area of 1.13 cm^2, which was appointed as YSZ800/CB (blank YSZ with carbon black annealed at 800 °C) to be compared with the other blank samples annealed at 900 and 1000 °C. Then, the best electrocatalytic activity sample of the YSZ/MCNSs and CSZ/MCNSs electrocatalysts was compared with its blank one.

3.3 Electro-chemical characterizations of the prepared electrocatalysts

For the evaluation of the electrocatalytic OER activity of YSZ/MCNSs and CSZ/MCNSs and their blank samples with carbon black, electrochemical measurements were assessed using the prepared composites as the working electrodes. OER measurements were performed between 0 and 0.9 V potential versus the silver/silver chloride couple reference electrode (Ag/AgCl) with saturated KCl filling solution and Pt wire as counter electrode at a scan rate of 5 mV/s in an oxygen-saturated alkaline electrolyte (0.1 M KOH). Electrochemical characterizations including cyclic voltammetry (CV), linear sweep voltammetry (LSV) and chrono-potentiometry were carried out on a VSP 300 potentiostat/galvanostat (BioLogic Science Instruments) electrochemical instrument using a three-electrode electrochemical system.

All potentials herein were converted versus the reversible hydrogen electrode (RHE) according to that reported in literature [13]. The potential for OER in alkaline medium (0.1 M KOH electrolyte), was calculated according to Eq. 1, and the overpotential was calculated by Eq. 2 [13].

$$E_{\text{vs.RHE}} = E_{\text{vs.Ag/AgCl}} + 1.009 \text{ V} \tag{1}$$

$$\eta = E_{\text{vs.RHE}} - 1.23 \text{ V} \tag{2}$$

4 Results and discussion

4.1 Physicochemical characterizations of the obtained composites

The morphologies and microstructures of the samples were characterized by Quanta FEG250 scanning electron microscopy SEM and FEG Tecnai Osiris transmission electron microscopy TEM. The SEM images of the molasses before annealing shown in Fig. 1, revealed the typical structures observed before for similar materials, with hollow microfibers of 50 to 100 μm diameters [14]. The fibers are composed of several combined tubes separated by 20–100 nm thick secondary walls. The outer wall of the microfibers is rough, with numerous cracks and flakes exfoliated out of the walls, reflecting the layered nature of the wall material. After annealing, YSZ/MCNSs with different carbon content at varied annealing temperatures under Ar are shown in Fig. 2, the fibrous structure gets completely destroyed into nanosheets with lateral diameters in the range of 20–100 nm [19–21]. The high pressure of the carbon and hydrocarbon gasses produced during the calcination process within the hollow fiber tubes is believed to be responsible for exfoliating the bio-fibers into nanosheets. The oxide particles seem to aggregate together into clusters of few micrometer sizes.

As shown in Fig. 3, CSZ nanoparticles are successfully synthesized and supported on the carbon nanosheets of molasses. It's observed that the oxide nanoparticles tend to aggregate together forming micrometer clusters. The blank sample of CSZ without CNSs displayed in Fig. 3k, l shows clusters of uniform spheres. Moreover, it can be observed that CSZ nanoparticles are randomly distributed on the surface of the molasses CNSs, and this in turn would further alleviate the aggregation of the nanoparticles and hence enhance the catalytic activity of the electrocatalysts. SEM images of CSZ and molasses microfibers (CSZ/MCFs) before annealing are shown in Fig. 4. It can be observed that the as-synthesized CSZ/MCFs composite via the
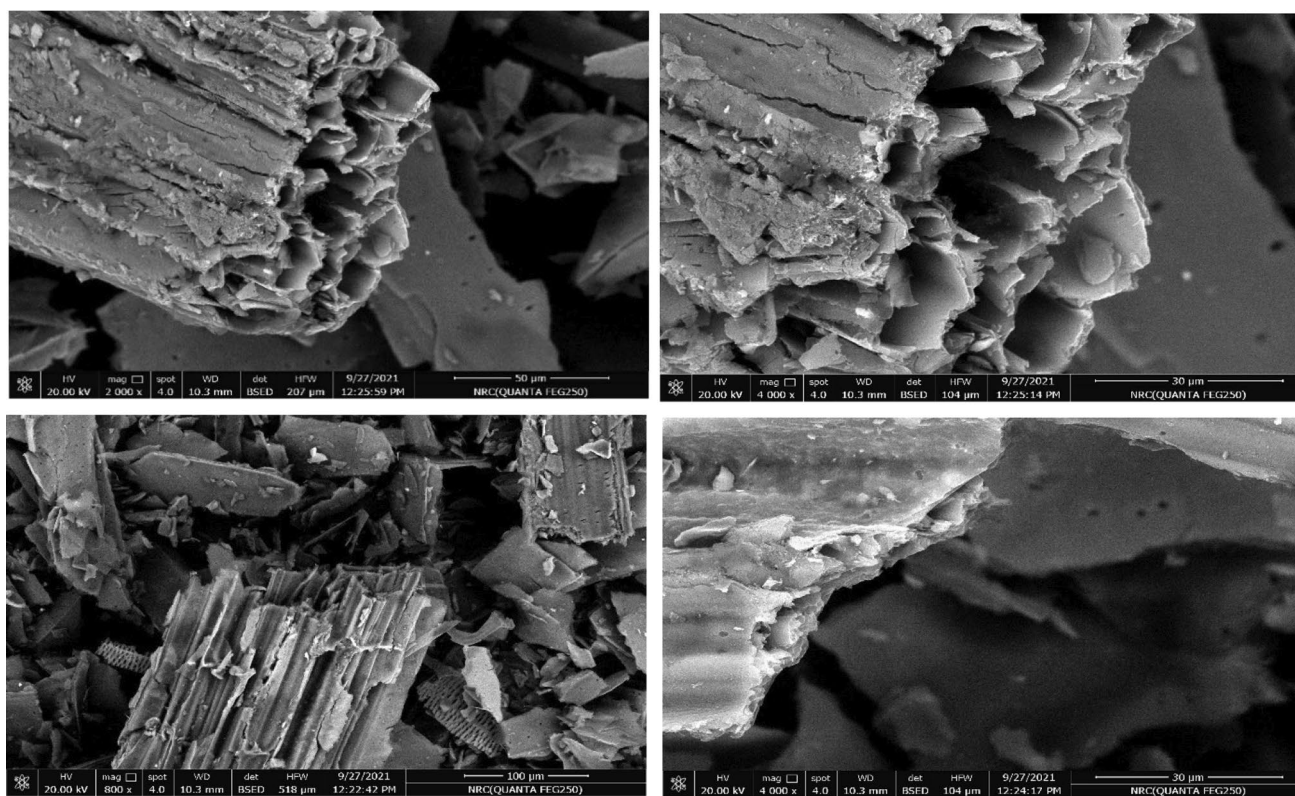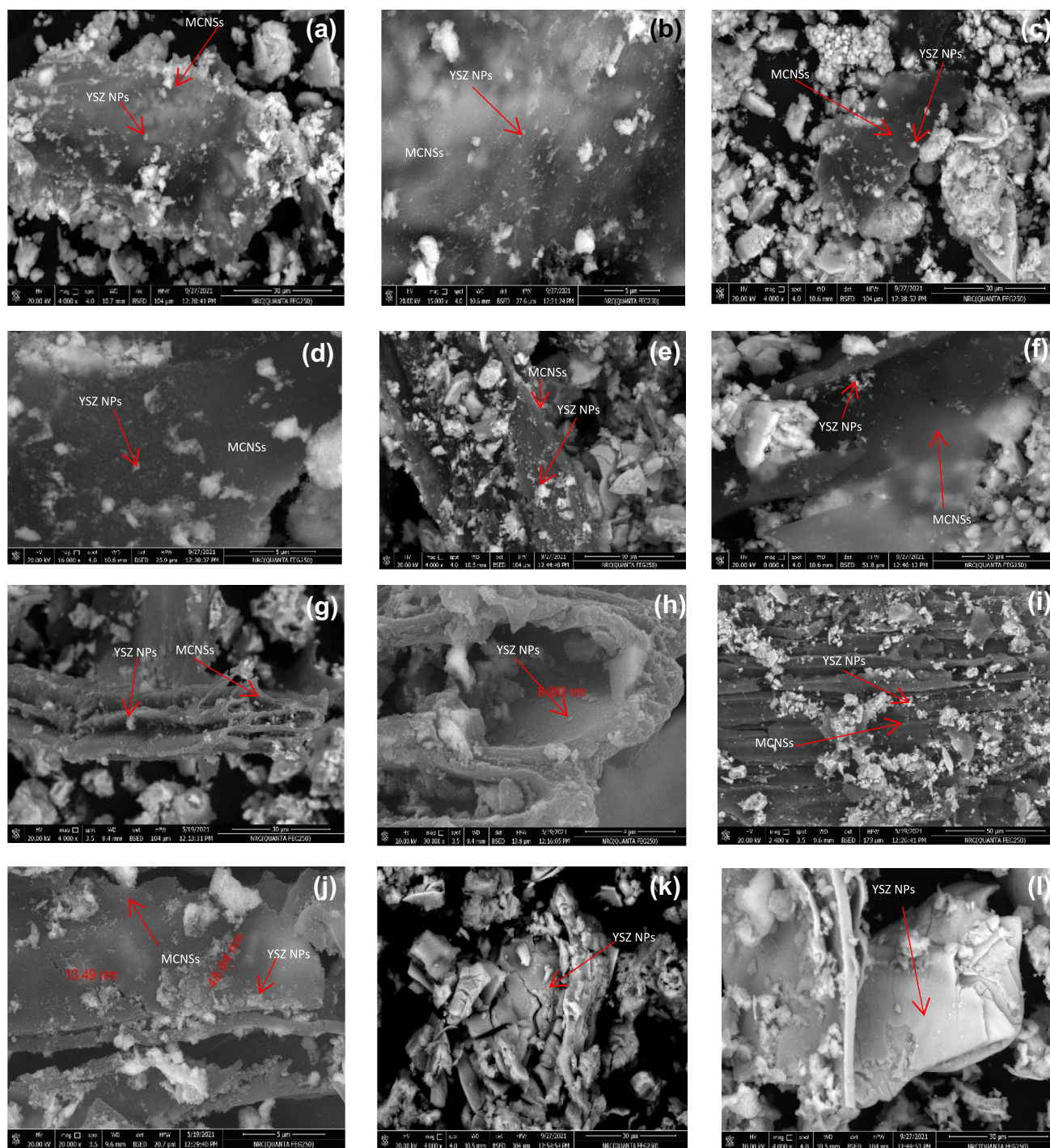

Fig. 1 SEM images of dried molasses carbon fibers at 200 °C for 3 h under vacuum
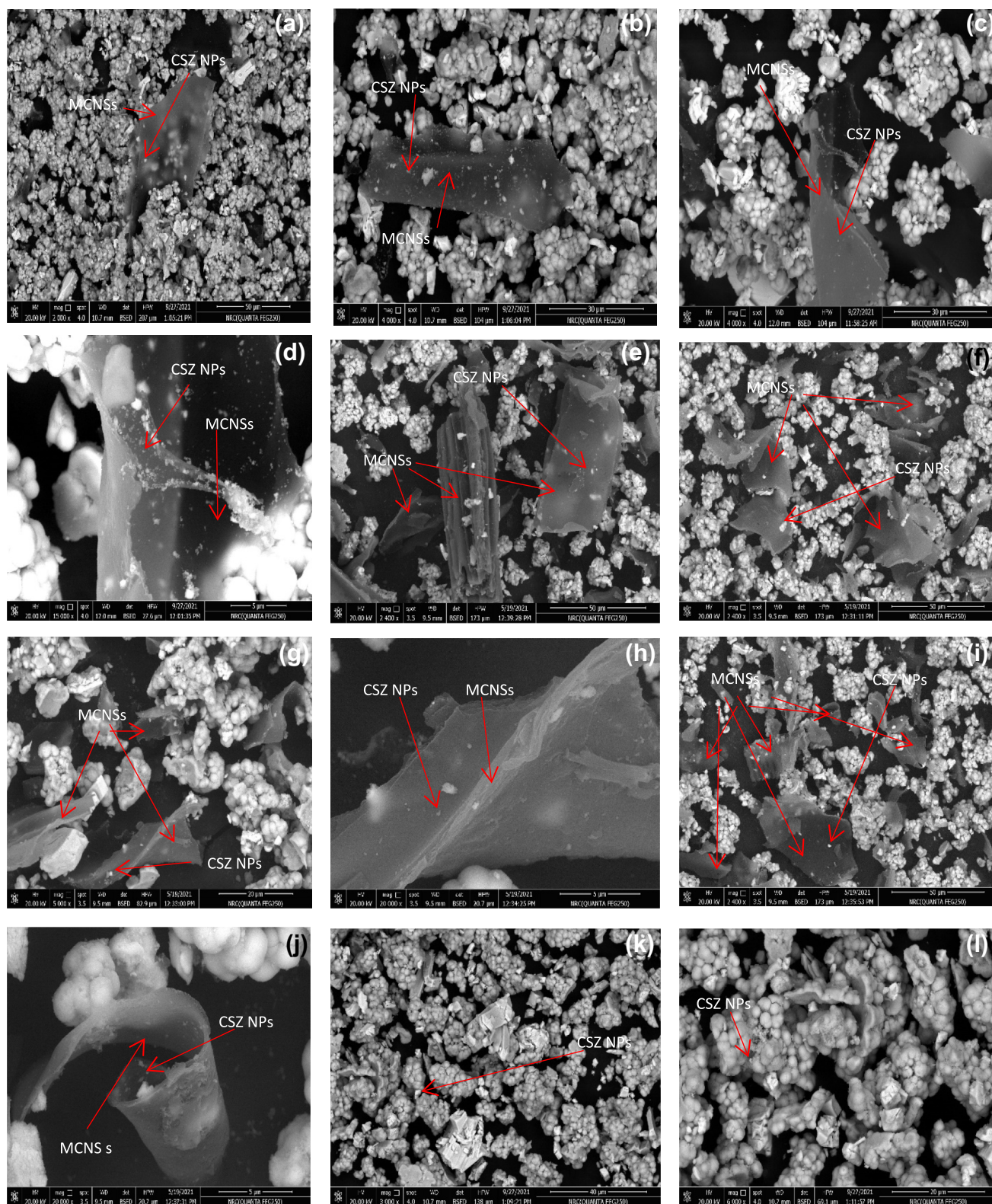
Fig. 2 SEM images of YSZ/CNSs catalysts after annealing under Ar **a, b** YSZ 800/mC 5% **c, d** YSZ 1000/mC 2% **e, f** YSZ 900/mC 10% **g, h** YSZ 900/mC 20% **i, j** YSZ 1000/mC 20% and **k, l** YSZ 800/CB

hydrothermal method are of cracked spherical shape and randomly distributed on the surface of the molasses carbon microfibers. More interestingly, as shown in Fig. 1, the morphology of these particles dramatically changes after annealing at higher temperatures under Ar from cracked spherical shape to a more uniform nanospheres aggregating together

forming clusters of few micrometers in size. It can be seen that the size of these nanoparticles is around 20–40 nm [22, 23].

Noteworthy the fact that the energy-dispersive X-ray analysis (EDX) can provide accurate information concerning the chemical composition and purity of the YSZ/

Fig. 3 SEM images of CSZ/CNSs catalysts after annealing under Ar **a, b** CSZ 1000/mC 2% **c, d** CSZ 800/mC 5% **e, f** CSZ 900/mC 20% **g, h** CSZ 900/mC 5% **i, j** CSZ 1000/mC 20% and **k, l** Blank CSZ 1000/CB
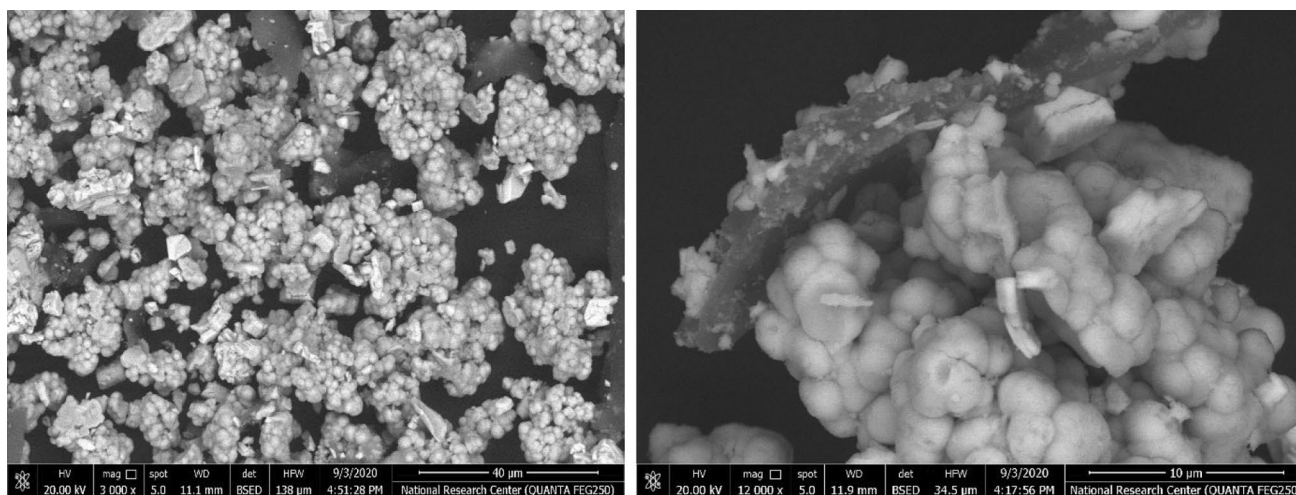
Fig. 4 SEM images of CSZ/MCFs before annealing at different magnifications

MCNSs and CSZ/MCNSs electrocatalysts [21, 23]. EDX spectra of YSZ/MCNSs and CSZ/MCNSs after annealing are shown in Fig. S3. These spectra show signals of Zr, Y, Ce, O and C while no other elements are detected, which indicates the successful preparation of the composites with no impurities and reveals that the samples are free of any contamination.

The TEM images of YSZ 800/mC 5% shown in Fig. 5 revealed that these clusters are composed of nanoparticles with 20–40 nm in size slightly sintered together. Strong
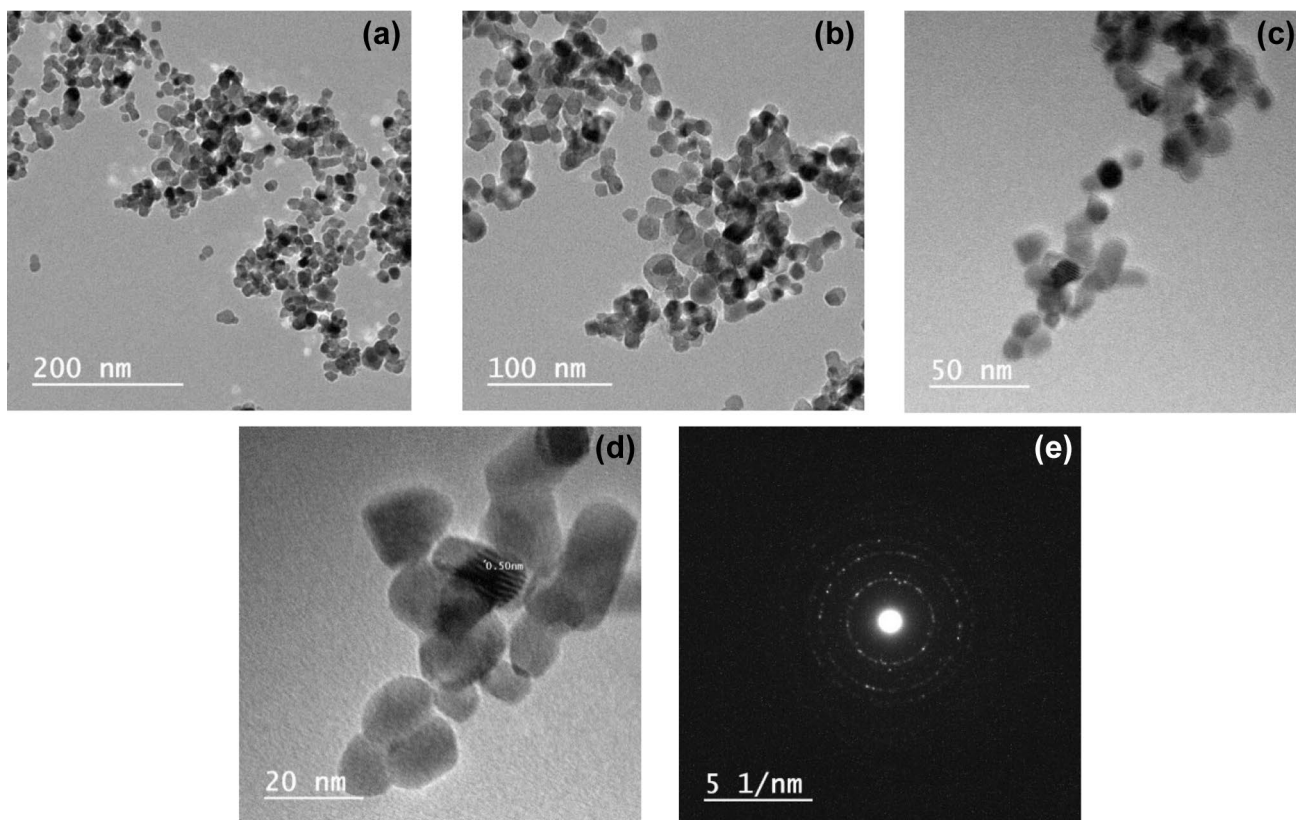
Fig. 5 TEM images of YSZ 800/mC 5% with scale bars **a** 200 nm **b** 100 nm **c** 50 nm and **d** 20 nm. **d** HR-TEM images of selected regions shown in c with *d* spacing of 0.50 nm indexed to the (200) planes of tetragonal YSZ and **e** Selected area electron diffraction pattern (SAED)

diffraction contrast arises from those particles in ideal Bragg orientation, and as Moire patterns are visible on some of them, the grains also seem to overlap. The crystallites do not feature a regular shape, while there are some that look approximately rectangular, most of them are in the form of rounded, irregular particles. The corresponding selected area electron diffraction pattern (SAED) revealed discrete spots, indicating the oxides nanoparticles are of good crystallinity. The high-resolution TEM (HR-TEM) image (Fig. 5d) revealed lattice fringes with an inter-planar spacing of 0.5 nm, which can be indexed to the (200) planes of the tetragonal YSZ [21, 22]. Since the ionic conductivity depends on the crystal structure, this high degree of ordering suggests good conductivity, which is bifacial for the electrocatalysts [24, 25].

Figure 6 shows TEM images of CSZ 1000/mC 2% and reveals that these clusters are composed of nanoparticles with size ranges from 20 to 60 nm. The HR-TEM image shown in Fig. 6d, reveals lattice fringes with an inter-planar spacing of 0.32 nm, which was indexed to the (111) planes of ceria [26]. TEM images reveal the relatively high surface area exposed for the OER. CSZ 1000/mC 2% has higher specific surface area when the content of carbon in the reactant is 2 wt%, which is more conductive to electrochemical processes. Therefore, active sites could be more exposed for enhancing the OER catalytic activity of this electrocatalyst with low carbon content. The selected area electron diffraction pattern (SAED) shown in Fig. 6e has discrete spots, which further demonstrates the crystalline character of the CSZ 1000/mC 2% oxide nanoparticles [27].

4.2 Boosted OER catalysis of YSZ/MCNSs and CSZ/MCNSs with their blank samples with carbon black

As shown in Fig. 7a, the overpotential at 20 mA cm^{-2} (η_{20}) of YSZ 800/mC 5% catalyst is as low as 79 mV, as it's the best electrocatalytic activity sample of the group of catalysts annealed at 800 °C with different molasses carbon weight ratios which are shown in Fig. S1. With the increase of the annealing temperature, the value of η_{20} increases. This catalyst exhibits the lowest η_{20} value of 79 mV at carbon loading of only 5 wt% and this η_{20} value is 391 mV lower than the blank YSZ 800/CB annealed at 800 ºC, indicating the role of the bio-derived nanosheets in enhancing the catalytic reaction. As shown in Fig. 7a, we also tested the OER catalytic
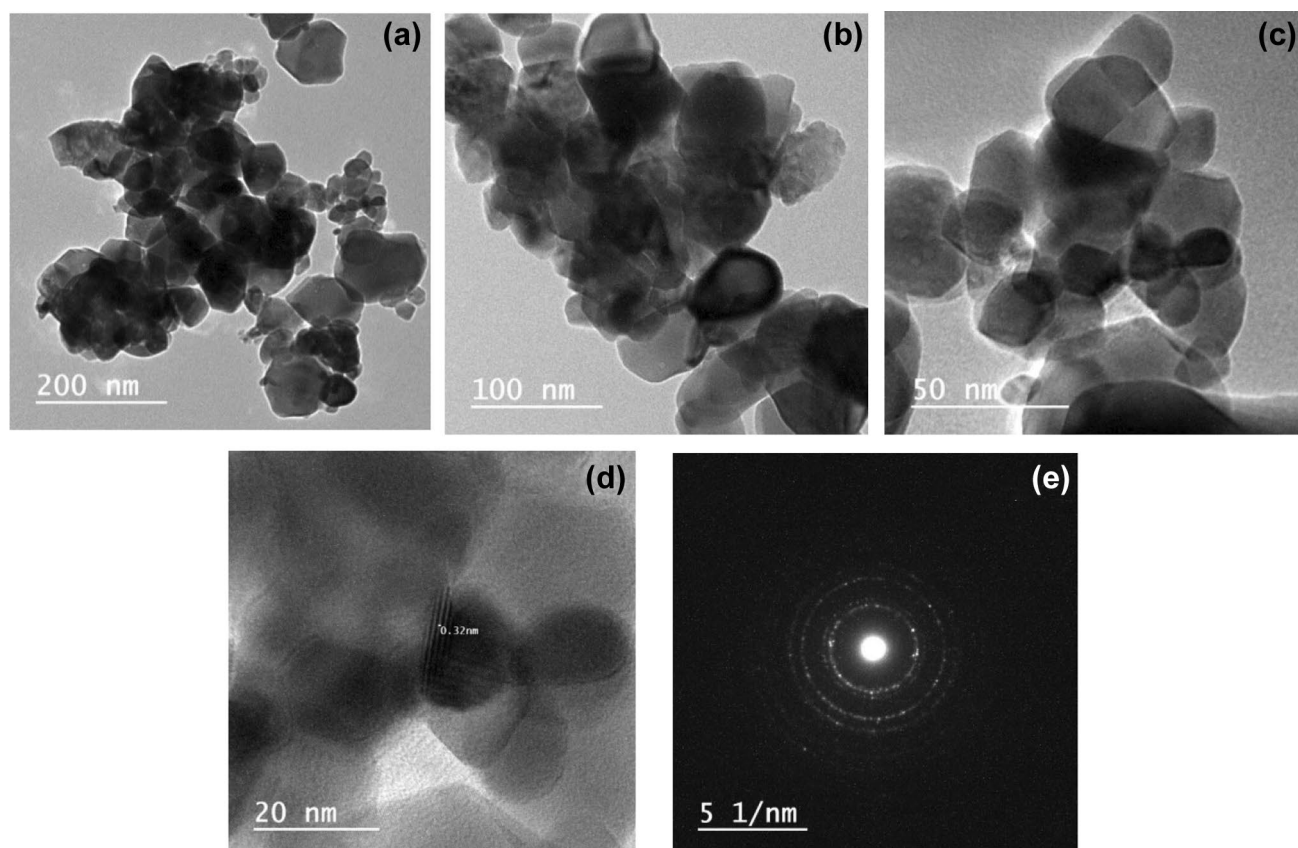
Fig. 6 TEM images of CSZ 1000/mC 2% with scale bars **a** 200 nm **b** 100 nm **c** 50 nm and **d** 20 nm. **d** HR-TEM images of selected regions shown in **c** with *d* spacing of 0.32 nm indexed to the (111) planes of ceria and **e** Selected area electron diffraction pattern (SAED)
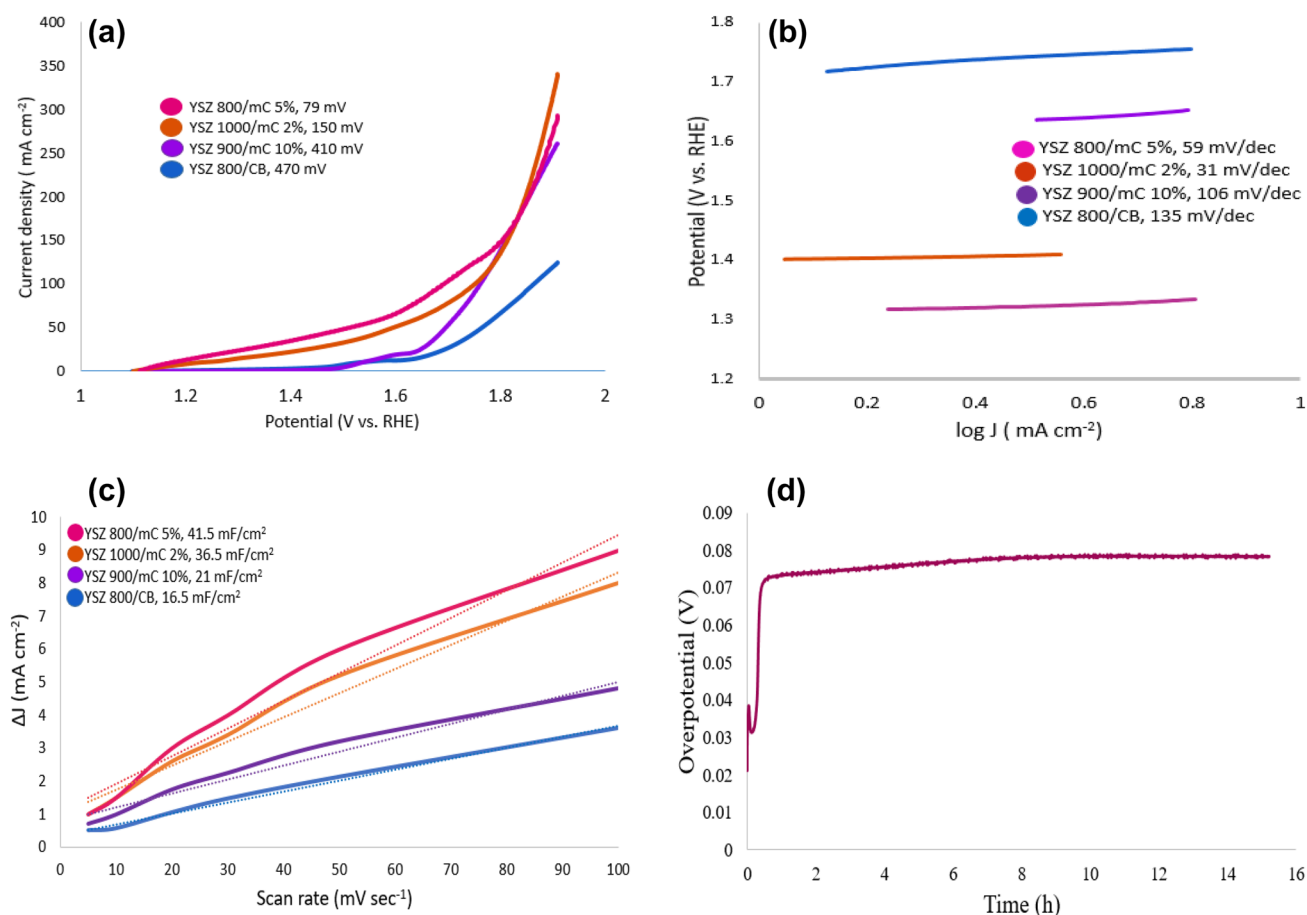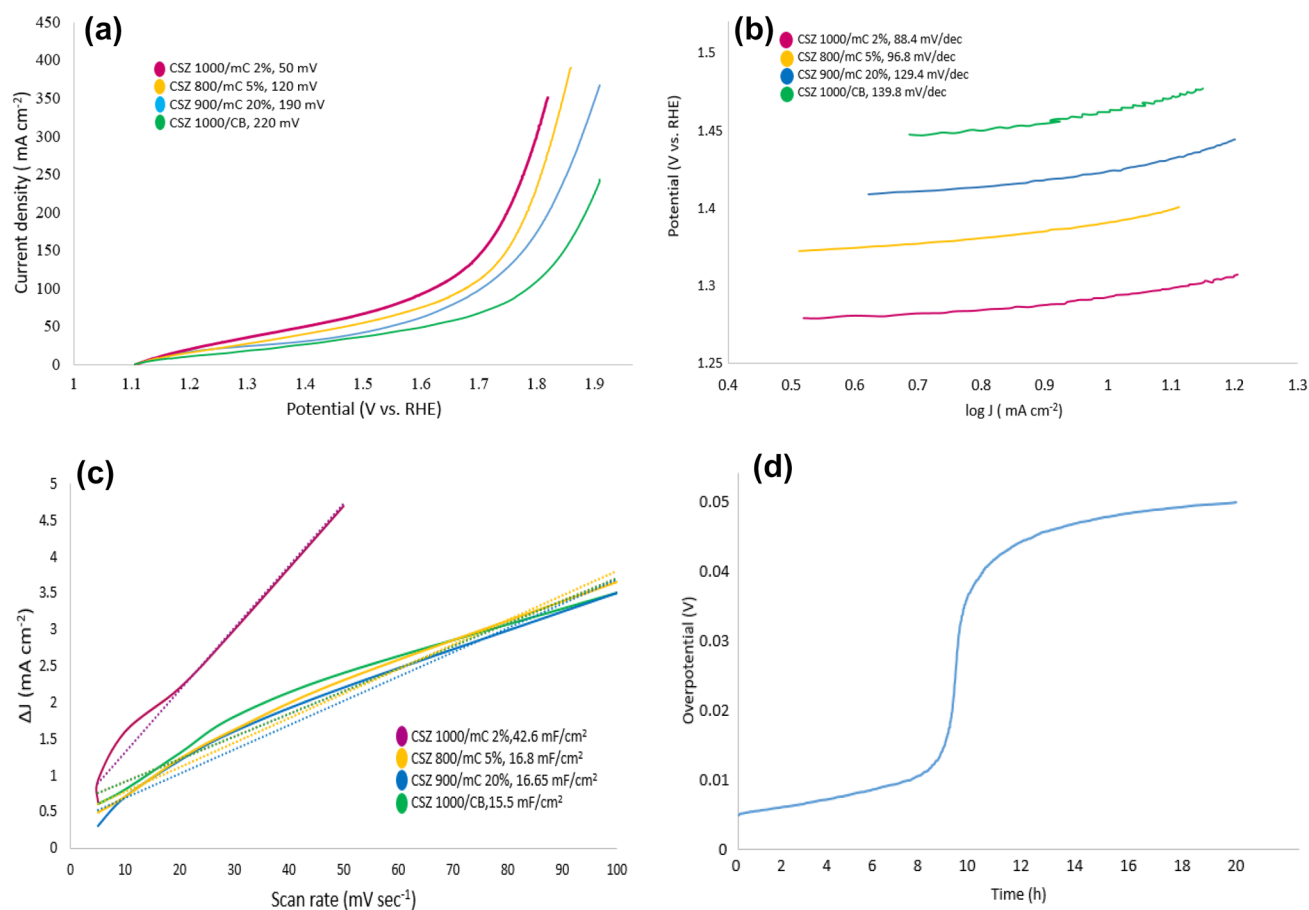
Fig. 7 OER performance of YSZ 800/mC 5%, YSZ 1000/mC 2%, YSZ 900/mC 10% and blank YSZ 800/CB catalysts in 0.1 M KOH **a** polarization curves **b** Tafel plots **c** Double layer capacitance C_{dl} and **d** Chronopotentiometry test of YSZ 800/mC 5%, 79 mV at 20 mA cm^{-2}

activity of the best catalysts of each group annealed at 900 and 1000 °C along with their blank samples annealed at the same temperatures, respectively, and they were found to be YSZ 1000/mC 2%, YSZ 900/mC 10% and YSZ 800/CB for comparison with the best electrocatalytic activity sample YSZ 800/mC 5%. Obviously, the YSZ 800/mC 5% catalyst could greatly enhance the OER process compared with the YSZ 1000/mC 2% (150 mV) and YSZ 900/mC 10% (410 mV) samples, both of which were superior to the blank YSZ 800/CB (470 mV).

For CSZ/MCNSs electrocatalysts, as shown in Fig. 8a, it can be observed from LSV curves that the composite sample CSZ 1000/mC 2% exhibits the lowest overpotential compared with the other composites including the blank one. It's obvious from Fig. S2 that CSZ 1000/mC 2% electrocatalyst was found to be the best electrocatalytic activity sample of the group of catalysts annealed at 1000 °C with different molasses carbon weight ratios. The lowest overpotential at the current density of 30 mA cm^{-2} is 50 mV for CSZ 1000/mC 2%, which is lower than that of CSZ 800/mC 5% (120 mV), CSZ 900/mC 20% (190 mV) and Blank CSZ

1000/CB (220 mV). It can be concluded that incorporation of only 2 wt% of molasses carbon into the CSZ composite while calcination at 1000 °C under Ar increases the OER activity compared with the other samples, and this in turn indicates that even incorporation of high amount of molasses carbon is better than carbon black CB effect on the electrocatalytic activity.

Furthermore, the Tafel analysis has been performed to assess the kinetic mechanism of the electrocatalyst during the OER process [28–31]. Tafel analysis was used to reveal the catalytic activity of the prepared electrocatalysts. From the polarization curves, Tafel plots were constructed from the linear region of the plot by plotting Overpotential versus Log (current density) and Tafel slopes were calculated. The plot of the Tafel slopes shown in Figs. 7b and 8b, was obtained from the polarization curves and calculated using the Tafel equation [29, 30]. The Tafel slopes of YSZ composites with bioderived nanosheets and those with carbon black shown in Fig. 7b, do not display a similar variation trend versus annealing temperature to that of LSVs. The Tafel slopes of the catalysts were compared, and were found

Fig. 8 OER performance of CSZ 1000/mC 2%, CSZ 800/mC 5%, CSZ 900/mC 20% and blank CSZ 1000/CB catalysts in 0.1 M KOH **a** Polarization curves **b** Tafel plots **c** Double layer capacitance C_{dl} and **d** Chronopotentiometry test of CSZ 1000/mC 2%, 50 mV at 30 mA cm^{-2}

to be: YSZ 800/mC 5% (59 mV/decade), YSZ 1000/mC 2% (31 mV/dec), YSZ 900/mC 10% (106 mV/dec), YSZ 800/CB (135 mV/dec). The relatively small Tafel slope revealed the rapid reaction kinetics and the highest electrochemical kinetics of the YSZ 800/mC 5% catalyst for OER catalysis. The results above show that moderate doping of MCNSs and annealing at 800 °C is beneficial to the improvement the OER activity of YSZ composites.

Similarly, it can be observed that the Tafel slopes of CSZ/MCNSs electrocatalysts perform the same variation trend as the corresponding polarization curves for each sample. As shown in Fig. 8b, the Tafel slope of CSZ 1000/mC 2% is 88.4 mV/dec, CSZ 800/mC 5% is 96.8 mV/dec, CSZ 900/mC 20% is 129.4 mV/dec and CSZ 1000/CB is 139.8 mV/dec. Once again, it seems that low amount of molasses carbon content leads to enhancing OER activity, however, in the case of the CSZ 900/mC 20% composite with higher amount of molasses carbon, it seems it decreases the OER activity. Overall, stabilized zirconia electrocatalysts doped with molasses carbon nanosheets seem to promote the oxygen evolution reaction with better activity than those with

carbon black. It can be concluded that the electrocatalyst CSZ 1000/mC 2% shows the highest OER activity in terms of the lowest overpotential and hence lowest Tafel slope.

The above results show that YSZ and CSZ composites with bio-derived carbon nanosheets have higher catalytic activities than other blank composites. The low catalytic activity observed for the blank YSZ 800/CB and CSZ 1000/CB suggested that Zr species have limited active sites. The SEM images in Fig. 2 show that the doping with molasses carbon changes the morphology of YSZ from a cracked micronized prismatic shape into nanosized near spherical structure with higher crystallinity which is confirmed by TEM. This transformation in morphology and crystallinity seems to activate more active sites on the surface. The changes in the particle size may also have an impact on the electrochemical surface area (ECSA).

Furthermore, in order to reveal the origins of the excellent OER activity of YSZ/MCNSs and CSZ/MCNSs electrocatalysts, the electrochemical double layer capacitance (C_{dl}) was calculated from the cyclic voltammograms (CV) curves at different scan rates of 5, 10, 20, 30, 50 and 100 mV/s, shown

in Fig. S4 and S5 within the potential window of 0–0.9 V vs. Ag/AgCl in the non-faradaic region. As a result, the electrochemical surface area (ECSA) was directly proportional to the C_{dl} and related to the performance of the catalyst [32].

As shown in Fig. 7c, the C_{dl} values of YSZ 800/mC 5% (41.5 mF cm^{-2}), YSZ 1000/mC 2% (36.5 mF cm^{-2}) and YSZ 900/mC 10% (21 mF cm^{-2}) were greater than that of YSZ 800/CB (16.5 mF cm^{-2}). The 3D porous structure of YSZ/MCNSs increases the ECSAs of YSZ 800/mC 5%, YSZ 1000/mC 2% and YSZ 900/mC 10% catalysts. The ECSA of YSZ 800/mC 5% catalyst almost double that of the YSZ composite with CB. Moreover, for CSZ/MCNSs electrocatalysts, their C_{dl} are shown in Fig. 8c, the linear slope of CSZ 1000/mC 2% was calculated to be 42.6 mF cm^{-2}, which is much higher than the C_{dl} values of the remaining electrocatalysts CSZ 800/mC 5%, CSZ 900/mC 20% and Blank CSZ 1000/CB with slopes 16.8, 16.65 and 15.5 mF cm^{-2}, respectively. Increasing the ECSA means more abundant active sites and facile electrolyte/catalysis interface processes. The intensified ECSA and abundant active sites accelerated the diffusion and adsorption of electrolytes and gaseous products, which also facilitated rapid charge transfer. This revealed that the intrinsic charge transfer could be accelerated by doping with MCNSs, which modulated the electronic structures of Y, Ce and Zr cations. Furthermore, the excellent electronic/ionic conductivity and high oxygen storage capacity of ceria also helps in enhancement of the OER electrochemical kinetics and activity [33, 34].

Therefore, the YSZ/MCNSs and CSZ/MCNSs electrocatalysts exhibited highly intrinsic catalytic activity for the OER. Thus, the superior catalytic activity of YSZ 800/mC 5% and CSZ 1000/mC 2% can be related to their higher ECSA.

The OER performance of YSZ 800/mC 5% and CSZ 1000/mC 2% is superior to that of blank YSZ 800/CB and blank CSZ 1000/CB, respectively, and comparable to that reported in the literature, as summarized in Table 1. It's necessary to perform the long-term stability and durability of the OER electrocatalysts to be used in practical applications. Thus, the stability of the best active electrocatalysts presented in this work is evaluated by chronopotentiometry (CP) which is the change in potential over time at constant driving current density. The long-term stability and durable performance of YSZ 800/mC 5% were evaluated by chronopotentiometry (CP) at 20 mA cm^{-2} for 15 h, as shown in Fig. 7d. After an activation period of less than 30 min, it seems that the overpotential of YSZ 800/mC 5% catalyst has a neglected attenuation, even for prolonged electrolysis of 15 h, indicating superior electrochemical stability and durability. The CP of CSZ 1000/mC 2% electrocatalyst was performed at a constant current density of 30 mA cm^{-2} for 20 h and shown in Fig. 8d. It is observed that the overpotential kept increasing for about 15 h until it reached a stable state and an overpotential of 50 mV at 30 mA cm^{-2} for up to 20 h. This also indicates the long-term stability and durability performance of CSZ 1000/mC 2% electrocatalyst which confirms the rapid charge transfer, facile gas adsorption and diffusion [28–37].

4.3 BET surface area analysis

Noteworthy, the electrochemical performance is affected by the specific surface area and pore volume of the electrocatalysts. In order to further investigate the surface area and porosity of the best electrocatalysts, N$_2$ adsorption and desorption measurements were performed. Figure 9 shows the N$_2$ adsorption–desorption isotherms and pore size distribution of the YSZ 800/mC 5% and CSZ 1000/mC 2% electrocatalysts. The adsorption–desorption isotherms of N$_2$ belong to the IUPAC IV isotherm type with hysteresis loops, which is characteristic of particles with uniform size and mesoporous structure. It's obvious that the catalysts showed type IV isotherms with hysteresis loop at a relative pressure of $P/P_0 = 0.45$ to 0.95 for the YSZ 800/mC 5% and CSZ 1000/mC 2% electrocatalysts. The presence of the hysteresis loops confirms the presence of mesopores in the electrocatalysts. The BET-specific surface area of the YSZ 800/mC 5% electrocatalyst was found to be 198.21 m^2 g^{-1}, the pore size was 5.3 nm, and the pore volume was 0.2753 cm^3 g^{-1}. While for the CSZ 1000/mC 2% electrocatalyst, the surface area was 173.35 m^2 g^{-1}, the pore size was 5.5 nm, and the pore volume was 0.2513 cm^3 g^{-1}. It is observed from the surface area data that the relatively high specific area of the electrocatalysts is one of the reasons for their high catalytic activity and these results are consistent with the TEM results. This high surface area may have originated from anchoring the YSZ and CSZ composites on the surface of the MCNSs. Furthermore, high surface area can provide more active sites for the electrochemical reactions and enhance the electrocatalytic activity and ease the diffusion of the gaseous products. The pore size distribution indicates the existence of the mesoporous structure and mesopores in the electrocatalysts [8, 35]. The high specific pore volume leads to the enhancement in faster charge and oxygen ions transportation and gaseous diffusion during the charge and discharge processes and thus providing high active sites for the electrochemical reactions and enhancing their performance. Therefore, the relatively high specific surface area and high specific pore volume lead to enhanced electrochemical activity and performance [38, 39] (Table 2).

4.4 Physicochemical characterizations of the best electrocatalysts

To further elucidate how molasses carbon nanosheets improve the OER activity of the studied electrocatalysts,

Table 1 Comparison of the electrochemical results with literature

Catalyst	Support	Electrolyte	Overpotential η (mV)	Tafel slope (mV/dec)	C_{dl} (mF cm^{-2})	Refs.
YSZ 800/mC 5%	Cu foil	0.1 M KOH	$\eta_{@20\,mA\,cm^{-2}}$ 79 mV	59	41.5	This work
YSZ 1000/mC 2%	Cu foil	0.1 M KOH	$\eta_{@20\,mA\,cm^{-2}}$ 150 mV	31	36.5	This work
YSZ 900/mC 10%	Cu foil	0.1 M KOH	$\eta_{@20\,mA\,cm^{-2}}$ 410 mV	106	21	This work
YSZ 800/CB	Cu foil	0.1 M KOH	$\eta_{@20\,mA\,cm^{-2}}$ 470 mV	135	16.5	This work
CSZ1000/mC 2%	Cu foil	0.1 M KOH	$\eta_{@30\,mA\,cm^{-2}}$ 50 mV	88.4	42.6	This work
CSZ 800/mC 5%	Cu foil	0.1 M KOH	$\eta_{@30\,mA\,cm^{-2}}$ 120 mV	96.8	16.8	This work
CSZ 900/mC 20%	Cu foil	0.1 M KOH	$\eta_{@30\,mA\,cm^{-2}}$ 190 mV	129.4	16.65	This work
CSZ 1000/CB	Cu foil	0.1 M KOH	$\eta_{@30\,mA\,cm^{-2}}$ 220 mV	139.8	15.5	This work
3D Zr-Co$_3$O$_4$/NF	Ni Foam	1 M KOH	$\eta_{@20\,mA\,cm^{-2}}$ 307 mV	99	114.3	[5]
Ru^0/CeO$_2$	GCE	0.5 M KOH	$\eta_{@10\,mA\,cm^{-2}}$ 420 mV	122	0.083	[6]
CeO$_2$/MOF/GO	GCE	1.0 M KOH	$\eta_{@10\,mA\,cm^{-2}}$ 386 mV	98.1	2.94	[8]
CeO$_2$/CuO/Co$_3$O$_4$	Cu Wire	0.1 M KOH	$\eta_{@10\,mA\,cm^{-2}}$ 520 mV	87.1	---	[17]
NiFeZr LDHs	Ni Foam	1 M KOH	$\eta_{@10\,mA\,cm^{-2}}$ 198 mV	53.1	4.16	[18]
NiFeZr MOFs-0.12	GCE	1 M KOH	$\eta_{@10\,mA\,cm^{-2}}$ 288 mV	66	0.18	[19]
Co/ZrO$_2$	GCE	1.0 M KOH	$\eta_{@10\,mA\,cm^{-2}}$ 373 mV	70.8	0.317	[27]
Co/CeO$_2$	GCE	1.0 M KOH	$\eta_{@10\,mA\,cm^{-2}}$ 365 mV	65.0	0.446	[27]
1-CeO$_2$@NGO	GCE	0.5 M KOH	$\eta_{@10\,mA\,cm^{-2}}$ 1.2 V	107	---	[29]
Ce$_{0.85}$Ni$_{0.15}$O$_2$	GCE	0.1 M KOH	η@1 mA cm^{-2} 560 mV	192	---	[35]
NF/CeO$_{2-x}$-Ni	Nickel Foam	6 M KOH	$\eta_{@50\,mA\,cm^{-2}}$ 390 mV	74	2.22	[37]
Ni80Fe20/50 wt% CeO$_2$	GCE	1 M KOH	$\eta_{@80\,mA\,cm^{-2}}$ 357 mV	40	---	[22]
Cu @ CeO2 @ NFC-0.25	Cu Foam	1 M KOH	$\eta_{@10\,mA\,cm^{-2}}$ 230.8 mV	32.7	2.74	[15]

The phase identification and the crystalline nature of the best of the studied electrocatalysts were confirmed by X-ray powder diffraction PXRD patterns which were performed by Philips diffractometer with monochromatic Cu K α radiation ($\lambda = 1.5405$ Å) and a fast multi-strip detector. X-ray diffractograms of the best electrocatalysts of YSZ/MCNSs; YSZ 800/mC 5%, YSZ 1000/mC 2%, YSZ 900/mC 10% are shown in Fig. S6 and the blank sample prepared without molasses carbon which is annealed at 800 °C is also shown for comparison.

All observed peaks of the YSZ/MCNSs electrocatalysts were indexed to 8 mol% yttria stabilized zirconia with a tetragonal phase without any observable impurities [38]. The XRD patterns were matched with the diffraction file of the zirconia tetragonal phase (YTZP) (ASTM file 00-049-1642) while no peaks corresponding to monoclinic

Table 2 The surface area data compared with literature

Sample	Surface area ($m^2\ g^{-1}$)	Refs.
YSZ 800/mC 5%	198.21	This work
CSZ 1000/mC 2%	173.35	This work
CMG-1	146.715	[8]
CeO_2	22.421	[8]
$CeO_2/CuO/Co_3O_4$	27.9	[17]
$Ce_{0.5}Ni_{0.5}O_2$	39	[35]
4YSZ	58	[38]
t-ZrO_2	74	[39]

zirconia were observed and the highest intensity peak observed at ca. 30° correspond to t (111) plane of tetragonal zirconia (space group: p 42/n m c) [22, 38]. In this study, the increase in oxygen vacancies may be due to the incorporation of carbon nanosheets from molasses in the YSZ lattice as observed in SEM. The characteristic peaks of YSZ/MCNSs composites match the tetragonal ZrO_2 phase (JCPDS 79-1764) in literature [22, 38, 40, 41]. The

broad peaks at $2\theta = 30.2°$, 50.3° and 60.2° are attributed to the (111), (112) and (121) lattice planes of tetragonal ZrO_2, respectively, and indicates the nanometer size of the particles. The XRD results demonstrate that our approach successfully stabilized the tetragonal phase of ZrO_2 in the electrocatalysts. Besides, there are no other impurity peaks are observed in the XRD patterns of YSZ/MCNSs catalysts, demonstrating that yttrium ions has been doped into the zirconia lattice [22]. XRD patterns of the remaining catalysts annealed at 900 and 1000 °C shows enlargement in the peak intensity as the annealed temperature increased, indicating the effect of thermal treatment of the samples on their catalytic activity.

These XRD patterns of the samples agrees well with that reported in the literature, suggesting the successful synthesis of YSZ doped with molasses carbon nanosheets. With the doping of molasses carbon, the crystallinity of YSZ increases but the main diffraction peaks still remain due to the larger size of Zr ion and its different coordination number, and this result is consistent with the TEM images [25, 41].
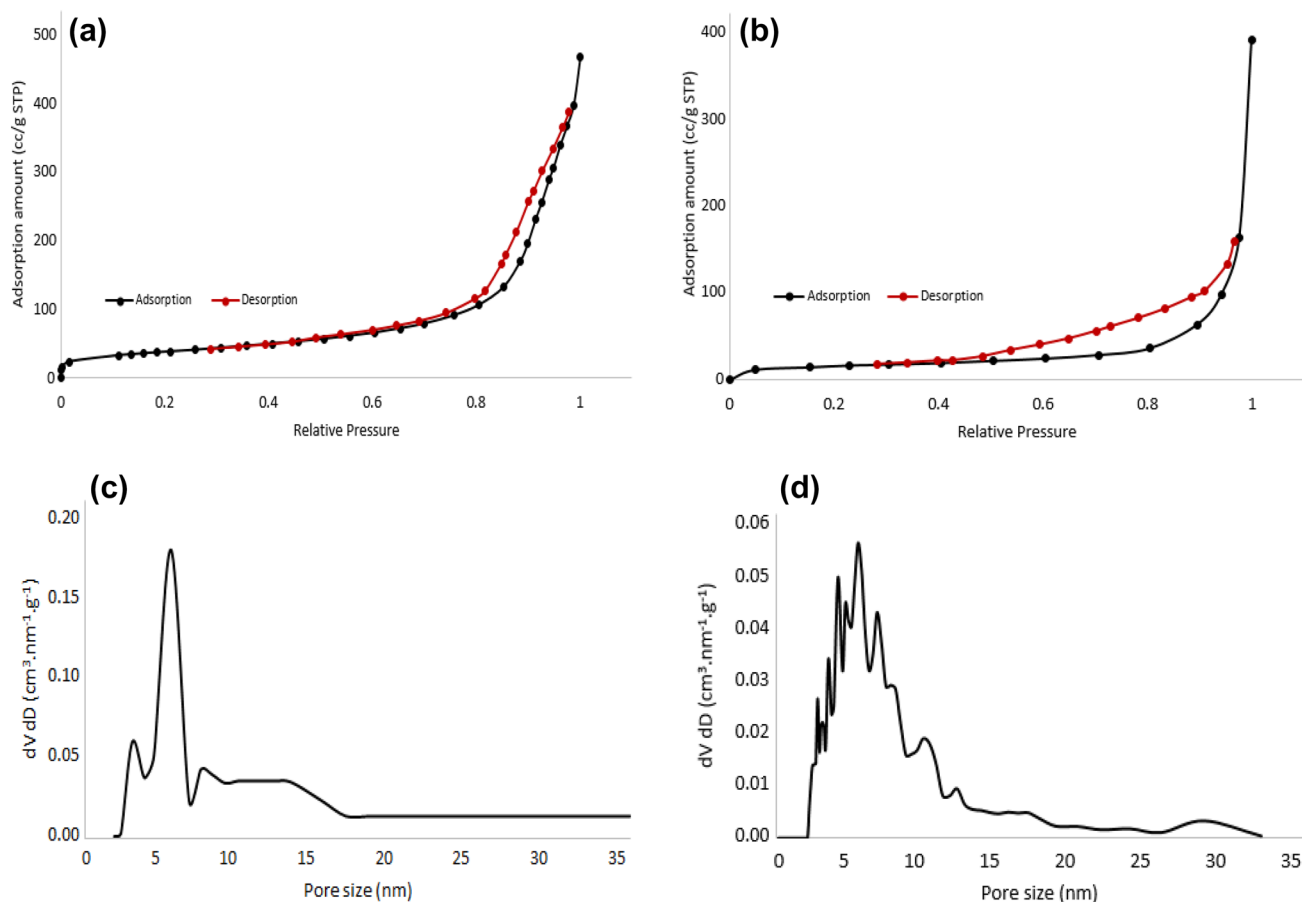
Fig. 9 N_2 adsorption–desorption isotherms of **a** YSZ 800/mC 5% and **b** CSZ 1000/mC 2%, and the pore size distribution of **c** YSZ 800/mC 5% and **d** CSZ 1000/mC 2%

Similarly, X-ray diffractograms of the best electrocatalysts of CSZ/MCNSs; CSZ 1000/mC 2%, CSZ 800/mC 5%, CSZ 900/mC 20% and the blank sample CSZ 1000/CB are shown in Fig. S7. It's obvious that the diffraction peaks in the XRD pattern of the CSZ nanoparticles exhibit both the tetragonal and cubic phases of the CSZ solid solution as the diffraction peaks observed at $2\theta = 28.47°$, $33.11°$, $47.48°$, $56.30°$, $59.07°$ and $69.44°$ correspond to (PDF#43-1002) of a cubic fluorite ceria structure and the diffraction peaks observed at $2\theta = 30.1°$, $35.0°$, $50.1°$ and $59.8°$ were assigned to the tetragonal zirconia phase (t-ZrO_2) (PDF#49-1642) [42, 43]. And these results are consistent with the TEM results.

Furthermore, in order to reveal the origins of the high catalytic activity of the YSZ 800/mC 5% and CSZ 1000/mC 2% electrocatalysts, the surface chemical and electronic states were analyzed by X-ray photoelectron spectroscopy tests on a PHI VersaProbe XPS system by Physical Electronics (PHI) with a detection limit of one atomic percent. XPS survey spectrum for YSZ 800/mC 5% catalyst is shown in Fig. 10a which displays the predominant diffraction peaks of Zr, Y, C and O which are present in the YSZ 800/mC 5% catalyst sample. The Zr 3d, C 1s, Y 3d and O 1s spectra of the YSZ 800/mC 5% catalyst are shown in Fig. 10b–e,

respectively, and no other impurities were detected. In XPS survey figure, the chemical species present in the YSZ/MCNSs composite surface can be distinguished, which are the zirconium (Zr 4p, 3d, 3p and 3s), yttrium (Y 3d), carbon (C 1s) and the oxygen (O 1s) signals [44]. The Zr $3d_{5/2}$ doublet peak found at a binding energy (BE) of 182.5 eV was related to Zr^{4+} state. The Y $3d_{5/2}$ and the O 1s BEs found at 159.5 and 532 eV, respectively, were associated to their oxide states [45]. The XPS analysis verified that YSZ/MCNSs composites were synthesized with a proportion of about 8 mol% Y_2O_3 in ZrO_2 with no contaminants [46]. A moderate peak of C 1s (285 eV) appears which indicates the presence of molasses carbon. As it is expected, annealing in an inert environment helped the presence of carbon without

Table 3 The atomic percentages of Zr, Y, C and O

Name	Peak BE	FWHM eV	Area (P) CPS.eV	Atomic %	Q
Zr 3d	185.4	5.63	433,334.8	22.06	1
O 1s	532.6	5.17	313,971	46.26	1
C 1s	286.96	5.3	80,884.73	30.44	1
Y 3d	159.45	4.45	12,420.54	1.24	1
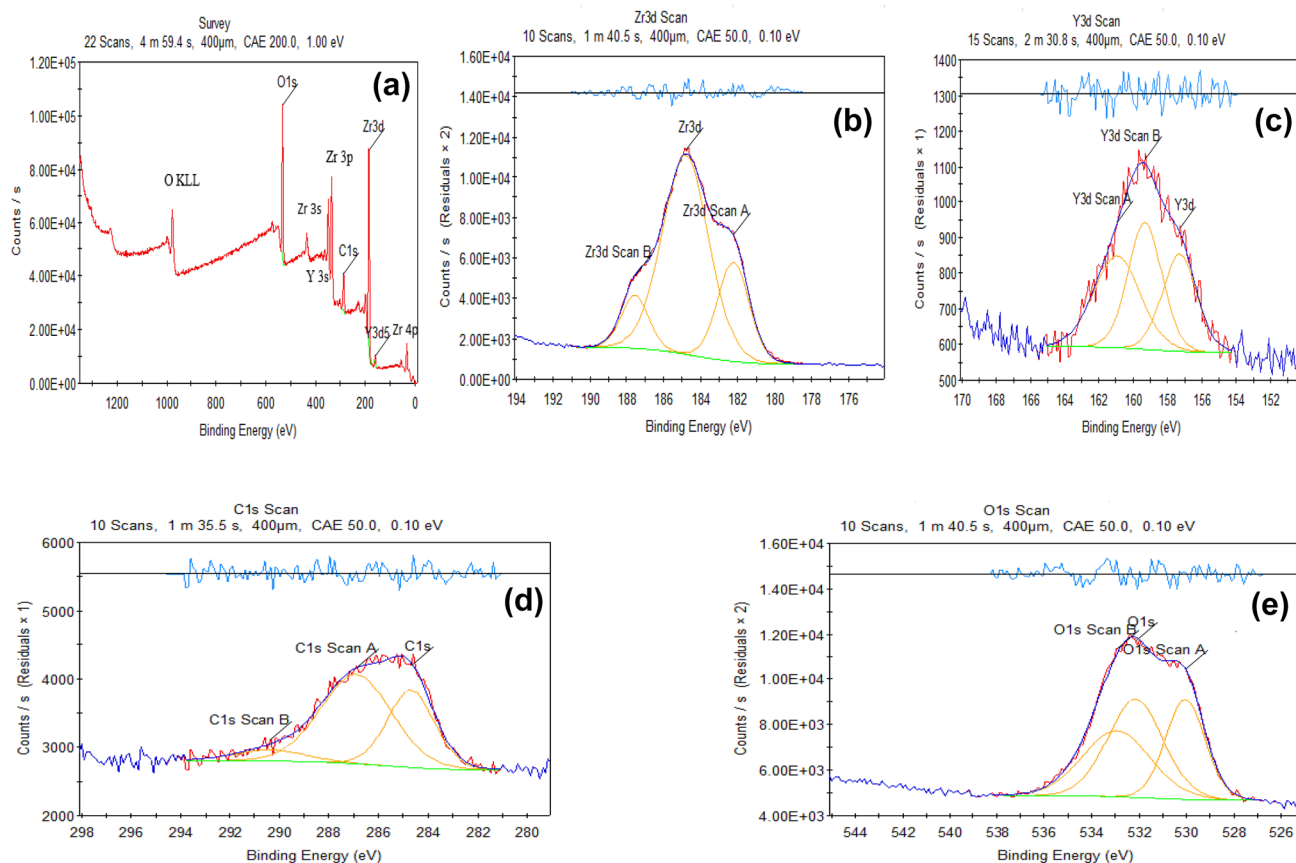
Fig. 10 XPS spectra of the YSZ 800/mC 5% electrocatalyst **a** The XPS profile survey spectra **b** Zr 3d **c** Y 3d **d** C 1s and **e** O 1s region spectra

oxidation. The atomic percentages of Zr, Y, O and C are shown in Table 3.

It is well-known that XPS is a very sensitive tool in analyzing the chemical state of zirconium cations in zirconia and its composites. Figure 10b displays the XPS spectra of the Zr 3d of the YSZ 800/mC 5% catalyst sample. XPS spectra of YSZ 800/mC 5% catalyst in the Zr 3d region show the presence of surface ZrO_2 and $Zr(OH)_4$ nanoparticles NPs. The peaks appeared at 184.82 and 182.23 eV are characteristic peaks of surface ZrO_2, whereas the peak at 187.56 eV is assigned to $Zr(OH)_4$ or bonding of zirconium with molasses carbon, which proves the successful doping of molasses carbon into the YSZ lattice [47, 48]. The binding energy values of Zr 3d components observed in this study are in accordance with values reported in the literature [44–51].

The Y 3d XPS spectrum shown in Fig. 10c exhibits two peaks at 157.3 and 159.32 eV, which are attributed to Y $3d_{5/2}$–O–Zr and Y $3d_{3/2}$–O–Zr, indicating the existence of Y^{3+} species. The third peak at a binding energy of 160.94 eV may be assigned to bonding of yttrium with molasses carbon Y $3d_{3/2}$–C, which proves the successful doping of molasses carbon into the YSZ lattice [39, 52, 53].

In order to illustrate the carbon bonding nature, a detailed analysis of the C 1s peak is presented in Fig. 10d. Figure 10d shows the C 1s spectra, which are decomposed into three Lorentzian peaks. Here, we focus on the two strongest peaks centered at 284.7 eV and 286.91 eV. This figure shows a typical XPS spectrum of C1s with the presence of a C–C peak around 284.7 eV which is characteristic for sp^2 bonded carbon atoms and demonstrate that the sp^2 bonds are dominant in the carbon layer on YSZ composite [54]. The oxidized species C–O are detected at a binding energy of around 287 eV or Zr–O–C formation and the peak appeared at binding energy value of 290.39 eV may be attributed to carbon–fluorine bonds [55–57].

In XPS spectra of O 1s core levels, shown in Fig. 10e, the three peaks at 530.05, 532.15 and 532.94 eV can be assigned to lattice oxygen, surface oxygen vacancy and adsorbed oxygen, respectively. It should be noted that the YSZ 800/mC 5% catalyst shows a higher concentration of oxygen vacancies or hydroxide ions on the surface, supposing that the incorporation of molasses carbon can create more oxygen vacancies and boost the adsorption/desorption of OH^- ions and thus accelerate the kinetic process leading to enhancement of the OER activity [58]. These results are in good agreement with literature as the deconvolution of O 1s spectrum resulted in the observation of O–Zr^{4+}, Zr–OH and C–OH or C–O–C bonds with binding energies in the range of 529.7 to 530 eV, 531.7 to 532 eV and 533 to 534 eV, respectively. XPS results proved the existence of oxygen vacancies in these composites pyrolyzed in inert atmosphere and the intensity of the peaks revealed surface defects with more surface hydroxide ions OH^- [59–63]. The above results

demonstrated the outstanding stability of the YSZ 800/mC 5% catalyst nanosheets and that there were stronger electronic interactions between Zr^{4+}, Y^{3+} and molasses carbon in YSZ 800/mC 5% catalyst with only 5 wt% molasses carbon. According to the above results and morphological analysis, YSZ 800/mC 5% electrocatalyst demonstrates excellent OER activity due to its unique nanosheet structure and Zr modified surface electronic structure. In addition, the unique morphology and binder-free copper foil substrate provide high conductivity and rapid charge transfer, which can expose more active sites. These can enhance intrinsic activity of the active sites to promote the OER catalytic performance.

Moreover, the survey spectrum of CSZ 1000/mC 2% electrocatalyst is shown in Fig. 11a and the atomic percentages of Zr, Ce, C and O elements are shown in Table 4, along with their peaks binding energies. The binding energy spectra of Zr $3d_{5/2}$ and Zr $3d_{3/2}$ are shown in Fig. 11b, three bands are observed at 182.01 eV, 184.63 eV and 187.46. The peaks located at 182.01 and 184.63 eV are characteristic peaks of surface ZrO_2, which corresponds to the Zr $3d_{5/2}$ and Zr $3d_{3/2}$, respectively, whereas the peak at 187.56 eV may be assigned to $Zr(OH)_4$ and the adsorption of OH^- ions on the catalyst surface which may be the reason of the high catalytic activity of the examined electrocatalyst [15, 64, 65].

Also, the Ce 3d state's spectra displayed in Fig. 11c, show different types of Ce 3d transitional peaks which were deconvoluted and analyzed in detail in the ceria-based catalysts in literature [65]. This proves that both Ce^{3+} and Ce^{4+} species co-exist in the catalyst.

The coexistence of Ce^{3+} and Ce^{4+} species provides more oxygen vacancies to the catalyst, which increases the conductivity and in turn leading to increase in the catalytic activity [15]. It's essential to mention that Ce^{4+} is reduced to Ce^{3+} and this reduction process is accompanied by the formation of oxygen vacancies, which helps in the transformation of adsorbed oxygen species into active oxygen species and also the migration of bulk lattice oxygen to the surface, which leads to enhancing the redox reaction [66]. Also, the formation energy for oxygen vacancies in CSZ catalysts indicates that the oxygen atoms, cerium and zirconium cations in CSZ solid solution could have been activated to show better charge mobility leading to optimized catalytic performance [67].

Moreover, C1s spectrum was deconvoluted to three peaks which arise from the CNSs structure as shown in Fig. 11d. The peak located at 284.51 eV is attributed to the C–C bond. The second peak located at 286.84 eV is assigned to the oxidized species C–O or Zr–O–C formation and the third one observed at 290.42 eV may be referred to –O–C=O group [68].

Additionally, the O 1s peaks of the CSZ 1000/mC 2% electrocatalyst all appear in the range of 530–533 eV; this binding energy range belongs to the adsorbed oxygen (O_{ads})
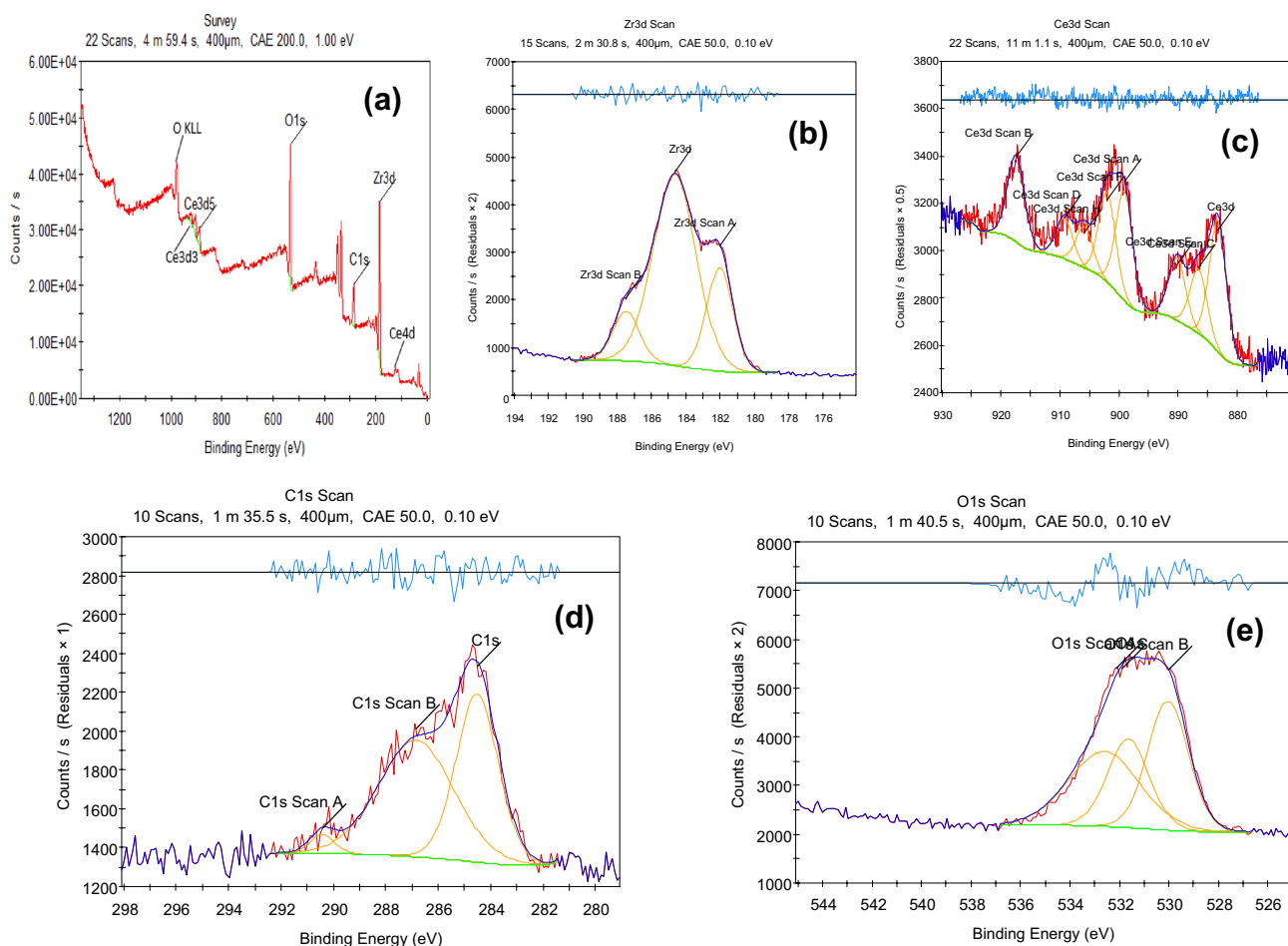
Fig. 11 XPS spectra of the CSZ 1000/mC 2% electrocatalyst **a** The XPS profile survey spectra **b** Zr 3d **c** Ce 3d **d** C 1s and **e** O 1s region spectra

Table 4 The atomic percentages of Zr, Ce, O and C

Name	Peak BE	FWHM eV	Area (P) CPS.eV	Atomic %	Q
O 1s	532.71	5.78	151,613.1	45.22	1
Zr 3d	185.3	5.88	173,814.4	17.91	1
C 1s	286.32	5.72	44,874.34	34.17	1
Ce 3d5	885.61	6.32	71,513.36	2.7	1

or oxygen defects on the electrocatalyst surface [69]. The O 1s XPS spectra of the sample shown in Fig. 11e, displays three oxygen states, among which the peak at the binding energy of 530.03 eV represents the lattice oxygen or oxygen combined with metal ions O–Ce–Zr. The characteristic peak at the binding energy of 531.89 eV represents the oxygen defects inside the lattice or oxygen of absorbed OH^- ions. The characteristic peak at the binding energy of 532.12 eV may be the oxygen bound to carbon O–C [70, 71].

It can be concluded that, the outstanding OER performance of the YSZ/MCNSs and CSZ/MCNSs catalysts can be ascribed to the synergistic effect of the components of the electrocatalyst; ceria, yttria, zirconia, and molasses carbon nanosheets, resulting in larger ECSA with sufficient active sites, which in turn leads to rapid charge transfer and facilitates oxygen and gaseous diffusion due to the presence of the oxygen vacancies.

5 Conclusion

Using YSZ and CSZ as representative examples of zirconia composites with metal oxides, YSZ and CSZ composites doped with molasses CNSs were synthesized. Herein, zirconia composites are converted into hydroxides under OER conditions which are responsible for the high catalytic activity of these composites in OER. Due to this in situ transformation, a current density of 20 mA cm^{-2} is obtained at much reduced overpotential of 79 mV in alkaline solution using YSZ 800/mC 5% catalyst and a current density of 30 mA cm^{-2} is obtained at overpotential of 50 mV using the CSZ 1000/mC 2% catalyst. The high catalytic activity, long-term stability, and durability of these catalysts were further

proved by electrochemical studies in terms of Tafel slopes, ECSA and chronopotentiometry. The experimental verifications indicate that the molasses CNSs doping in YSZ and CSZ composites led to the optimization of the morphology and electronic structure of this unique nanosheet structure, and so OER performance. This work may provide a guide for designing better metal oxide-based nanomaterials as efficient electrocatalysts with high catalytic activity.

Supplementary Information The online version contains supplementary material available at https://doi.org/10.1007/s10800-023-01980-2.

Declarations

Competing interests The authors declare that they have no conflicts of interest in this work.

References

1. Xu X, Pan Y, Lei Ge et al (2021) High-performance perovskite composite electrocatalysts enabled by controllable interface engineering. Small 17:2101573. https://doi.org/10.1002/smll.202101573

2. Fei L, Sun H, Xu X et al (2023) Understanding the bifunctional catalytic ability of electrocatalysts for oxygen evolution reaction and urea oxidation reaction: recent advances and perspectives. Chem Eng J 471:144660. https://doi.org/10.1016/j.cej.2023.144660

3. Kiriya D, Lobaccaro P, Nyein HYY et al (2016) General thermal texturization process of MoS_2 for efficient electrocatalytic hydrogen evolution reaction. Nano Lett 16:4047–4053. https://doi.org/10.1021/acs.nanolett.6b00569

4. Murata T, Kotsuki K, Murayama H et al (2019) Metal-free electrocatalysts for oxygen reduction reaction based on trioxotriangulene. Commun Chem 2:46. https://doi.org/10.1038/s42004-019-0149-9

5. Yang G, Zhu B, Fu Y et al (2021) High-valent zirconium-doping modified Co_3O_4 weave-like nanoarray boosts oxygen evolution reaction. J Alloys Compd 886:161172. https://doi.org/10.1016/j.jallcom.2021.161172

6. Demir E, Akbayrak S, Önal AM, Özkar S (2019) Ceria supported Ruthenium(0) nanoparticles: highly efficient catalysts in oxygen evolution reaction. J Colloid Interface Sci 531:570–577. https://doi.org/10.1016/j.jcis.2018.07.085

7. Luo S, Li X, Wang M et al (2020) Long-term electrocatalytic N_2 fixation by MOF-derived Y-stabilized ZrO_2: insight into the deactivation mechanism. J Mater Chem A 8:5647–5654. https://doi.org/10.1039/D0TA01154A

8. Chen Y, Huang N, Liang Y (2021) Preparation of CeO_2/Cu-MOF/GO composite for efficient electrocatalytic oxygen evolution reaction. Ionics 27:4347–4360. https://doi.org/10.1007/s11581-021-04173-z

9. Liang X, Wang Q, Liu Sh et al (2021) Shape control of exposed planes in ceria-zirconia based electrocatalysts for methanol oxidation. Int J Hydrogen Energy 46:27483–27494. https://doi.org/10.1016/j.ijhydene.2021.06.030

10. Ding Y, Jia Y, Jiang M et al (2021) Superior catalytic activity of Pd-based catalysts upon tuning the structure of the ceria-zirconia support for methane combustion. Chem Eng J 416:129150. https://doi.org/10.1016/j.cej.2021.129150

11. Li F, Li Y, Song Zh et al (2015) Evolution of the crystalline structure of zirconia nanoparticles during their hydrothermal synthesis and calcination: insights into the incorporations of hydroxyls into the lattice. J Eur Ceram Soc 35:2361–2367. https://doi.org/10.1016/j.jeurceramsoc.2015.02.017

12. Ramos-Garcés MV, Sanchez J, Kálery La Luz-Rivera KL et al (2020) Morphology control of metal-modified zirconium phosphate support structures for the oxygen evolution reaction. Dalton Trans 49:3892–3900. https://doi.org/10.1039/C9DT04135D

13. Xu X, Song F, Hu X (2016) A nickel iron diselenide-derived efficient oxygen-evolution catalyst. Nat Commun 7:12324. https://doi.org/10.1038/ncomms12324

14. Fidelis MEA, Pereira ThVC, Gomes OFM et al (2013) The effect of fiber morphology on the tensile strength of natural fibers. J Mater Res Technol 2:149–157. https://doi.org/10.1016/j.jmrt.2013.02.003

15. Xia J, Zhao H, Huang B et al (2020) Efficient optimization of electron/oxygen pathway by constructing ceria/hydroxide interface for highly active oxygen evolution reaction. Adv Funct Mater 30:1908367. https://doi.org/10.1002/adfm.201908367

16. Li Ch, Sun Y, Hess F et al (2018) Catalytic HCl oxidation reaction: stabilizing effect of Zr-doping on CeO_2 nano rods. Appl Catal B 239:628–635. https://doi.org/10.1016/j.apcatb.2018.08.047

17. Shaghaghi Z, Jafari S, Mohammad-Rezaei R (2022) The heterostructure of ceria and hybrid transition metal oxides with high electrocatalytic performance for water splitting and enzyme-free glucose detection. J Electroanal Chem 915:116369. https://doi.org/10.1016/j.jelechem.2022.116369

18. Li R, Wang Y, Li W et al (2019) Ternary NiFeZr layered double hydroxides: a highly efficient catalyst for the oxygen evolution reaction. Chem Commun 55:13370–13373. https://doi.org/10.1039/C9CC06219J

19. Wang Y, Tang W, Li X, Wei D (2021) Improving the electrocatalytic activity of NiFe bimetal-organic framework toward oxygen evolution reaction by Zr doping. Electrochim Acta 381:138292. https://doi.org/10.1016/j.electacta.2021.138292

20. Yuan Y, Wang J, Adimi S et al (2019) Zirconium nitride catalysts surpass platinum for oxygen reduction. Nat Mater 19:282–286. https://doi.org/10.1038/s41563-019-0535-9

21. Demir E, Akbayrak S, Önal AM, Özkar S (2018) Titania, Zirconia and Hafnia supported Ruthenium(0) nanoparticles: highly active

hydrogen evolution catalysts. J Colloid Interface Sci 531:570–577. https://doi.org/10.1016/j.jcis.2018.07.085

22. Cossar E, Agarwal K, Nguyen VB et al (2021) Highly active nickel-iron nanoparticles with and without ceria for the oxygen evolution reaction. Electrocatalysis 12:605–618. https://doi.org/10.1007/s12678-021-00674-7

23. Xing F, Ma J, Ki S et al (2022) High-entropy intermetallics on ceria as efficient catalysts for the oxidative dehydrogenation of propane using CO_2. Nat Commun 13:5065. https://doi.org/10.1038/s41467-022-32842-8

24. Benck JD, Hellstern ThR, Jakob Kibsgaard J et al (2014) Catalyzing the Hydrogen Evolution Reaction (HER) with molybdenum sulfide nanomaterials. ACS Catal 4:3957–3971. https://doi.org/10.1021/cs500923c

25. Gruber H, Hryha E, Lindgren K et al (2022) The effect of boron and zirconium on the microcracking susceptibility of IN-738LC derivatives in laser powder bed fusion. Appl Surf Sci 573:151541. https://doi.org/10.1016/j.apsusc.2021.151541

26. Mathew S, Hosseinirad E, Kim KC et al (2022) Enhanced electrocatalytic water splitting by Sm and Gd-doped ceria electrocatalysts on Ni foam substrate. Electrochim Acta 435:141382. https://doi.org/10.1016/j.electacta.2022.141382

27. Akbayrak M, Önal AM (2021) Metal oxides supported cobalt nanoparticles: active electrocatalysts for oxygen evolution reaction. Electrochim Acta 393:139053. https://doi.org/10.1016/j.electacta.2021.139053

28. Jin-Tao Ren JT, Yuan GG, Ch WC et al (2018) Rationally designed Co_3O_4-C nanowire arrays on Ni foam derived from metal organic framework as reversible oxygen evolution electrodes with enhanced performance for Zn-air batteries. ACS Sustain Chem Eng 6:707–718. https://doi.org/10.1021/acssuschemeng.7b03034

29. Kashinath L, Byrappa K (2022) Ceria boosting on in situ nitrogen-doped graphene oxide for efficient bifunctional ORR/OER activity. Front Chem 10:889579. https://doi.org/10.3389/fchem.2022.889579

30. Zheng W, Liu M, Lee LYS (2020) Best practices in using foam-type electrodes for electrocatalytic performance benchmark. ACS Energy Lett 5:3260–3264. https://doi.org/10.1021/acsenergylett.0c01958

31. Mehboob A, Gilani SR, Anwar A et al (2021) Nanoscale cobalt-oxide electrocatalyst for efficient oxygen evolution reactions in alkaline electrolyte. J Appl Electrochem 51:691–702. https://doi.org/10.1007/s10800-021-01529-1

32. Li Q, Wang X, Tang K et al (2017) Electronic modulation of electrocatalytically active center of Cu_7S_4 nanodisks by cobalt-doping for highly efficient oxygen evolution reaction. ACS Nano 11:12230–12239. https://doi.org/10.1021/acsnano.7b05606

33. Liu Y, Li Y, Wu Q et al (2021) Hollow CoP/FeP_4 heterostructural nanorods interwoven by CNT as a highly efficient electrocatalyst for oxygen evolution reactions. Nanomater 11:1450. https://doi.org/10.3390/nano11061450

34. Dhanasekaran P, Williams ShR, Kalpana D, Bhat SD (2018) Boosting efficiency and stability using zirconia nanosphere-held carbon for proton exchange membrane fuel cells. RSC Adv 8:472–480. https://doi.org/10.1039/C7RA10509F

35. Milikić J, Fuentes RO, Tasca JE et al (2022) Nickel-doped ceria bifunctional electrocatalysts for oxygen reduction and evolution in alkaline media. Batteries 8:100. https://doi.org/10.3390/batteries8080100

36. Ali Z, Mehmood M, Ahmad J et al (2021) Fluorine doped CNTs for efficient OER activity outperforming iridium supported carbon electrocatalyst. J Appl Electrochem 51:1573–1581. https://doi.org/10.1007/s10800-021-01600-x

37. Yu J, Wang Zh, Wang J et al (2020) The role of ceria in a hybrid catalyst toward alkaline water oxidation. Chemsuschem 13:5273–5279. https://doi.org/10.1002/cssc.202001542

38. Lee J-H, Kim M, Lim S et al (2022) Yttria-stabilized zirconia of balanced acid-base pair for selective dehydration of 4-methyl-2-pentanol to 4-methyl-1-pentene. Catalysts 12:559. https://doi.org/10.3390/catal12050559

39. Basahel SN, Ali TT, Mokhtar M et al (2015) Influence of crystal structure of nanosized ZrO_2 on photocatalytic degradation of methyl orange. Nanoscale Res Lett 10:73. https://doi.org/10.1186/s11671-015-0780-z

40. Koo JY, Hwang S, Ahn M et al (2016) Controlling the diameter of electrospun yttria-stabilized zirconia nanofibers. J Am Ceram Soc 99:3146–3150. https://doi.org/10.1111/jace.14331

41. Molina-Reyes J, Tiznado H, Soto G et al (2018) Physical and electrical characterization of yttrium-stabilized zirconia (YSZ) thin films deposited by sputtering and atomic-layer deposition. J Mater Sci 29:15349–15357. https://doi.org/10.1007/s10854-018-8909-3

42. Teeparthi SR, Awin EW, Kumar R (2018) Dominating role of crystal structure over defect chemistry in black and white zirconia on visible light photocatalytic activity. Sci Rep 8:5541. https://doi.org/10.1038/s41598-018-23648-0

43. Götsch Th, Wallisch W, Stöger-Pollach M et al (2016) From zirconia to yttria: sampling the YSZ phase diagram using sputter-deposited thin films. AIP Adv 6:025119. https://doi.org/10.1063/1.4942818

44. Ouyang J, Zhao Z, Yang H et al (2019) Surface redox characters and synergetic catalytic properties of macroporous ceria-zirconia solid solutions. J Hazard Mater 366:54–64. https://doi.org/10.1016/j.jhazmat.2018.11.083

45. Rodriguez MA, Anunziata OA, Beltramone AR, Martínez ML (2021) Multiple-wall carbon nanotubes obtained with mesoporous material decorated with ceria-zirconia. Mater Lett 283:128900. https://doi.org/10.1016/j.matlet.2020.128900

46. Colomer MT, Simenas M, Banys J et al (2022) Effect of sintering under $CO+N_2/H_2$ and CO_2+air atmospheres on the physico-chemical features of a commercial nano-YSZ. J Alloys Compd 904:163976. https://doi.org/10.1016/j.jallcom.2022.163976

47. Ramírez EB, Huanosta A, Sebastian JP et al (2007) Structure, composition and electrical properties of YSZ films deposited by ultrasonic spray pyrolysis. J Mater Sci 42:901–907. https://doi.org/10.1007/s10853-006-0004-0

48. Huang L, Chen D, Luo G et al (2019) Zirconium-regulation-induced bifunctionality in 3D cobalt-iron oxide nanosheets for overall water splitting. Adv Mater 31:1901439. https://doi.org/10.1002/adma.201901439

49. Stevie FA, Donley CL (2020) Introduction to x-ray photoelectron spectroscopy. J Vac Sci Technol A 38:063204. https://doi.org/10.1116/6.0000412

50. Subramaniam KM, Rao LLR, Jampana N (2015) Inductively coupled reactive ion etching studies on sputtered yttria stabilized zirconia thin films in SF_6, Cl_2, and BCl_3 chemistries. J Vac Sci Technol B 33:022003. https://doi.org/10.1116/1.4907707

51. Ram S, Mondal A (2004) X-ray photoelectron spectroscopic studies of Al^{3+} stabilized t-ZrO_2 of nanoparticles. Appl Surf Sci 221:237–247. https://doi.org/10.1016/S0169-4332(03)00883-3

52. Zhu J, Zhu Y, Shen W et al (2011) Growth and characterization of yttrium oxide films by reactive magnetron sputtering. Thin Solid Films 519:4894–4898. https://doi.org/10.1016/j.tsf.2011.01.049

53. Cheng X, Qi Z, Zhang G et al (2009) Growth and characterization of Y_2O_3 thin films. Physica B 404:146–149. https://doi.org/10.1016/j.physb.2008.10.022

54. Liu M, Liu W, Liu X et al (2019) Yttrium oxide as a Q-switcher for the near-infrared erbium-doped fiber laser. Nanophotonics 9:0563. https://doi.org/10.1515/nanoph-2019-0563

55. Ermolieff A, Chabli A, Pierre F et al (2001) XPS, Raman spectroscopy, X-ray diffraction, specular X-ray reflectivity, transmission electron microscopy and elastic recoil detection analysis of emissive carbon film characterization. Surf Interface Anal 31:185. https://doi.org/10.1002/sia.955

56. Jerng SK, Seong YuD, Hong Lee J et al (2011) Graphitic carbon growth on crystalline and amorphous oxide substrates using molecular beam epitaxy. Nanoscale Res Lett 6:565. https://doi.org/10.1186/1556-276X-6-565

57. Morgan DJ (2021) Comments on the XPS analysis of carbon materials. C 7:51. https://doi.org/10.3390/c7030051

58. Park J, Back T, Mitchel W et al (2015) Approach to multifunctional device platform with epitaxial graphene on transition metal oxide. Sci Rep 5:14374. https://doi.org/10.1038/srep14374

59. Kitzmann J, Göritz A, Fraschke M et al (2016) Perfluorodecyltrichlorosilane-based seed-layer for improved chemical vapour deposition of ultrathin hafnium dioxide films on graphene. Sci Rep 6:29223. https://doi.org/10.1038/srep29223

60. Cubillos GI, Romero E, Umaña-Perez A (2021) ZrN-ZrOxNy vs ZrO$_2$-ZrOxNy coatings deposited via unbalanced DC magnetron sputtering. Sci Rep 11:18926. https://doi.org/10.1038/s41598-021-98052-2

61. Ran J, Wang T, Zhang J et al (2020) Modulation of electronics of oxide perovskites by sulfur doping for electrocatalysis in rechargeable Zn-air batteries. Chem Mater 32:3439. https://doi.org/10.1021/acs.chemmater.9b05148

62. Takayanagi M, Tsuchiya T, Minohara M et al (2017) Surface electronic structure of proton-doped YSZ thin film by soft-X-ray photoemission spectroscopy. J Soc Mater Sci Jpn 42:61. https://doi.org/10.14723/tmrsj.42.61

63. Zhu W, Nakashima Sh, Marin E et al (2021) Annealing-induced off-stoichiometric and structural alterations in Ca^{2+} and Y^{3+} stabilized zirconia ceramics. Mater 14:19. https://doi.org/10.3390/ma14195555

64. Wang H, Han X, Zhang L et al (2021) Integrating ceria with cobalt sulfide as high-performance electrocatalysts for overall water splitting. Fundam Res 17:47. https://doi.org/10.1016/j.fmre.2021.12.008

65. Grewal S, Andrade AM, Liu Z et al (2020) Highly active bifunctional oxygen electrocatalytic sites realized in ceria-functionalized graphene. Adv Sustain Syst 4:2000048. https://doi.org/10.1002/adsu.202000048

66. Yu J, Wang J, Long X et al (2021) Formation of FeOOH nanosheets induces substitutional doping of CeO$_{2-x}$ with high-valence Ni for efficient water oxidation. Adv Energy Mater 11:2002731. https://doi.org/10.1002/aenm.202002731

67. Dai T, Zhang X, Sun M et al (2021) Uncovering the promotion of CeO$_2$/CoS$_{1.97}$ heterostructure with specific spatial architectures on oxygen evolution reaction. Adv Mater 33:2102593. https://doi.org/10.1002/adma.202102593

68. Zhou X, Guo S, Cai Q, Huang S (2019) Ceria/cobalt borate hybrids as efficient electrocatalysts for water oxidation under neutral conditions. Nanoscale Adv 1:3686–3692. https://doi.org/10.1039/C9NA00356H

69. Ma Y, Burye TE, Nicholas JD (2021) Pt current collectors artificially boosting praseodymium doped ceria oxygen surface exchange coefficients. J Mater Chem A 9:24406–24418. https://doi.org/10.1039/D1TA06237A

70. Galani SM, Mondal A, Srivastava DN, Panda AB (2020) Development of RuO$_2$/CeO$_2$ heterostructure as an efficient OER electrocatalyst for alkaline water splitting. Int J Hydrogen Energy 45:18635–18644. https://doi.org/10.1016/j.ijhydene.2019.08.026

71. Woo S, Lee J, Lee DS et al (2020) Electrospun carbon nanofibers with embedded co-ceria nanoparticles for efficient hydrogen evolution and overall water splitting. Mater 13:856–866. https://doi.org/10.3390/ma13040856

Publisher's Note Springer Nature remains neutral with regard to jurisdictional claims in published maps and institutional affiliations.

Authors and Affiliations

Menna M. Abo-Zeid[1] · Muhammad G. Abd El-Moghny[2] · H. Shawkey[3] · A. M. Daher[1] · Amr M. Abdelkader[4] · Mohamed S. El-Deab[2]

✉ Muhammad G. Abd El-Moghny
mugamal@cu.edu.eg

✉ Mohamed S. El-Deab
msaada68@yahoo.com

1 Nuclear Materials Authority, Cairo, Egypt

2 Department of Chemistry, Faculty of Science, Cairo University, Cairo, Egypt

3 Department of Microelectronics, Electronics Research Institute (ERI), Giza, Egypt

4 Department of Design and Engineering, Bournemouth University, Poole, UK